

Chapter 5

Beamforming to enhance specular reflection from bone surfaces

Contents

5.1	Introduction	4
5.2	Specular beamforming for homogeneous media	6
5.2.1	Geometrical considerations	6
5.2.2	The specular signature	8
5.2.3	Model of specular transform	13
5.2.4	Model-based characterization of the specular reflection	17
5.3	Refraction-corrected specular beamforming for multi-layered media	19
5.3.1	Geometrical considerations	19
5.3.2	The specular signature in presence of refraction	21
5.3.3	Model of specular transform	24
5.4	The impact of pore scattering on the contrast of specular images: a 2D simulation study	27
5.4.1	Materials & methods	27
5.4.2	Results	31
	Parametric results on the presences of specular structures.	31
	Specular images compared to DAS image.	34
5.4.3	Summary and discussion.	38
5.5	Conclusion	40

Abstract

5.1 Introduction

Throughout the history of ultrasound imaging, beamforming has played a crucial role in revealing the medium's reflectivity and is primarily responsible for image formation. Traditionally, most beamforming algorithms (beamformers) apply delays and weights to received backscattered signals, using the average as an estimate of reflectivity. The probe is virtually oriented to a specific point on the medium (corresponding to a pixel in the image) using chosen delays and weights.

In medical ultrasound imaging, DELAY-AND-SUM (DAS) [1] is the most widely used and robust beamformer for image reconstruction. The center frequencies employed in medical ultrasound typically range from 2 to 15 MHz [2]. Beamformers based on DAS assume a homogeneous medium composed only of point scatterers, indicating that all scatterers in the medium are considered small compared to the wavelength. Consequently, the signal is backscattered uniformly in all directions. In this scenario, the majority of the backscattered energy is concentrated around receivers proximal to the lateral position of the scatterer (see Figure 5.1a). With this assumption, the choice of weights does not depend on the received data but relies solely on the directivity of the receiving elements, leading to data-independent beamforming.

DAS beamforming can yield good image quality for specular objects parallel to the surface of the ultrasound probe. In this scenario, the interface is considered as a large number of adjacent small scatterers. However, when the interface is not parallel to the probe surface, the propagation direction of the reflected wavefront is no longer uniform. According to the Snell-Descartes law on specular reflection, the reflection direction depends on the incident angle and the orientation of the specular interface. If the receive subaperture is centered around the lateral position of the pixel to be reconstructed, a significant portion of the back-scattered energy is lost (see Figure 5.1b).

Cortical bone is the seat of both specular and diffuse scattering. The cortical pores and trabeculae, forming the microstructure, act as scatterers smaller than the wavelength. On the external (periosteal) and internal (endosteal) surfaces of the cortex, the large impedance ratio between soft tissue and bone tissue leads to specular reflection. Therefore, during ultrasound imaging of cortical bone, the significance of specular scattering cannot be overlooked.

As discussed in Chapters 1 and 3, achieving a high-quality image of the cortex is crucial for clear visualization of the periosteal and endosteal surfaces. Specifically, Chapter 3 highlighted that during DAS beamforming, diffuse signals from the microstructure create speckle that may obscure the specular signal from the endosteal surface of the bone. Thus, an adaptive reconstruction technique is necessary to enhance signals from both the external and internal surfaces of cortical bone. Consequently, the optimal image reconstruction of bone cortex interfaces requires the application of an adaptive receive sub-aperture determined by exploiting properties of specular reflection. . In this chapter, we present the design of a specialized beamforming algorithm. This algorithm is tailored to physics of specular reflection and refraction, with the specific goal of accentuating the external and internal interfaces of the bone cortex.

In recent years, various approaches have been proposed for extracting specular information in medical ultrasound imaging. In 2008, *Vogt et al.* [3] suggested

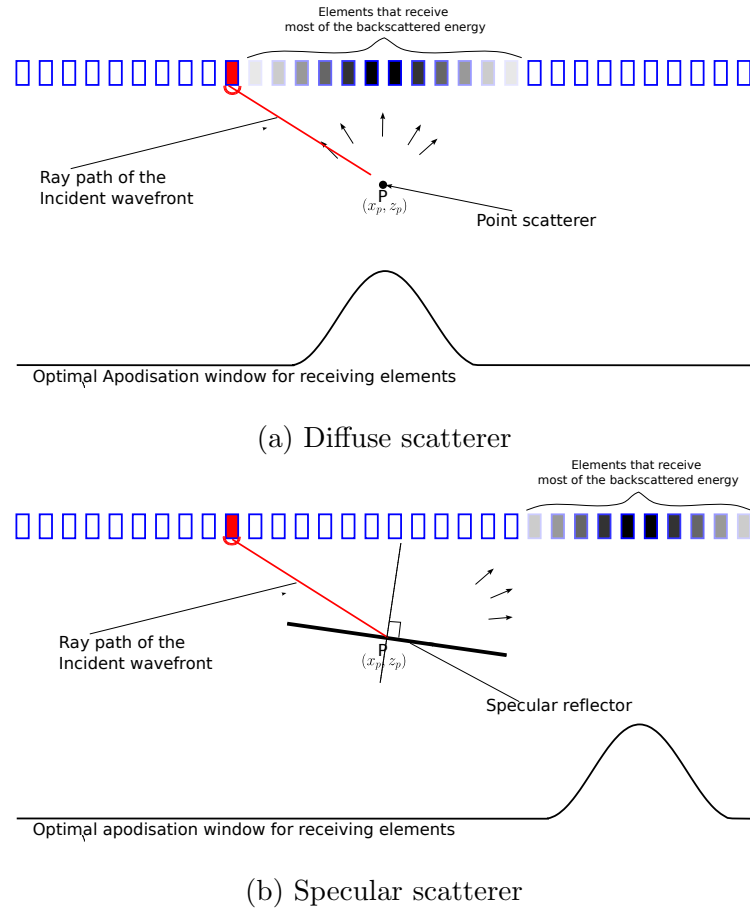


Figure 5.1: Illustration of the optimal receive sub-aperture for the reconstruction of pixel P . In (a) a small point scatterer lies at the pixel whereas in (b) a tilted specular interface passes through the pixel. In (a) most of the back-scattered energy is concentrated to receivers around the lateral position of the pixel. In (b), the back-scattered energy shows directivity and is no longer focused around the lateral position of the pixel.

exploiting the laws and properties of specular reflections characterized by high amplitude and directionality following Snell's law, to reconstruct parametric images. These images contain first-order statistics such as mean, standard deviation, maximum, and minimum across all emission-reception events of specular reflections. By analyzing the parametric images, specular reflection could be effectively differentiated from diffuse scattering. This method utilized a single-element transducer. Similarly, *Bandaru et al.* [4] proposed using an array transducer to enhance reflections from specular interfaces. Instead of using the average, as in DAS methods, they took the standard deviation of received backscattered signals across the receive aperture. The orientation of the specular interface was estimated based on the peak echo amplitude. This method was developed for conventional focusing.

For synthetic focusing scheme, *Rodriguez-Molares et al.* [5] proposed a technique of emphasizing specular reflection for needle tracking using a synthetic aperture sequence. Their technique, based on the source-image principle, involves developing a specular reflection model. They compare this model with the coherent compound-ing of received signals that follow Snell's law to obtain a matched filter maximizing the signal-to-noise ratio (SNR) of signals reflected by planar interfaces. This

technique suppresses speckle and enhances the visualization of specular interfaces, such as an inserted needle. In a similar manner *Malamal et Panicker* [6] proposed a data-dependent apodisation tuned for specular reflection. They used Coherent Plane Wave Compounding to apply DAS beamforming where for each pixel, an adapted receive subaperture and window depending on the similarity of the received backscattered signals is determined. More recently, *Malamal et al.* [7] proposed an innovative approach involving the radon transform and plane wave imaging to identify the receiver index that maximizes the back-scattered energy from a specular interface. Then, a receive apodization window, centered around this optimized receiver index, is selected during Delay-and-Sum (DAS) beamforming.

In a preliminary study, \textit{Nagaoka et al.}[8] suggested the use of a data-independent apodization weight to highlight both diffuse scattering from small heterogeneities and specular reflection from flat interfaces.

Recently, *Malamal and Panicker* [9] proposed to provide a real-time visual feedback mechanism for operators. They introduced a color-coded image containing a vectorized estimation of the reflection directivity within a defined region of interest. This allows the operator to reorient the probe or adjust the transmission sequence to align parallel to the surface of the reflector. Employing a plane wave imaging sequence, they applied this method to synthetic and experimental data for needle tracking and external bone surface imaging, effectively distinguishing fractured and smoothed regions of the periosteal surface of a bone.

However, like conventional DAS algorithms, all these methods assume a homogeneous medium and a straight ray-path propagation hypothesis. To emphasize the reflection of the external and internal surfaces of the bone, it is necessary to take into account the physics of reflection and refraction. Recently, *Renaud et al.* [10] and *Nguyen et al.* [11] suggested algorithms for imaging within the bone cortex, taking into account refraction. It's important to note that the specularity of bone surfaces is not considered in the proposed algorithms.

The rest of the chapter is organized as follows. In section 5.2 we will explain the specular reflection principle for a flat interface in a homogeneous medium. In the next section 5.3, we will explain the principle of the method developed during the thesis for a multilayer medium with curved interfaces. Section 5.4 is the application of the developed method to synthetic ultrasound data and in section 5.5 we discuss the method and conclude.

5.2 Specular beamforming for homogeneous media

In this section we describe the principle of specular beamforming and the physics behind this principle as it is described by Rodriguez-Molares et al. [5] for the visualisation of needle inserted inside a homogeneous medium.

5.2.1 Geometrical considerations

We will assume in the rest of the chapter that we are using a single element transmission technique with t designating the index of the transmitting element and r the index of the receiving element. The signals recorded by the elements are stored

in the 3D-matrix \mathbf{S} . The dimensions of this matrix are $[N \times N_r \times N_t]$ where N is the number of samples, N_r is the number of receiving elements and N_t is the number of transmissions.

Let us consider a medium to be imaged containing a θ -oriented plane reflector passing through the pixel $P \equiv (x_P, z_P)$. The equation of this reflector is given by:

$$(D_s) : z = -\tan(\theta)(x - x_P) + z_P \quad (5.1)$$

An ultrasound probe is placed on the surface of the medium (at depth $z=0$). Suppose an ultrasound ray (T) originating from element $t \equiv (x_t, z_t)$ of the probe, incident on point P of the interface and (R) is the reflected ray from P to receiving element $r \equiv (x_r, z_r)$. According to the law of specular reflection, the reflected ray corresponding to a specular reflection (R_s) is symmetric to the incident ray T from the normal interface. We note α_s the angle between the incident ray and the normal to the specular interface passing through P . Therefore, the angle between (R_s) and the normal of the specular interface is $-\alpha_s$ (see Panel 5.2b).

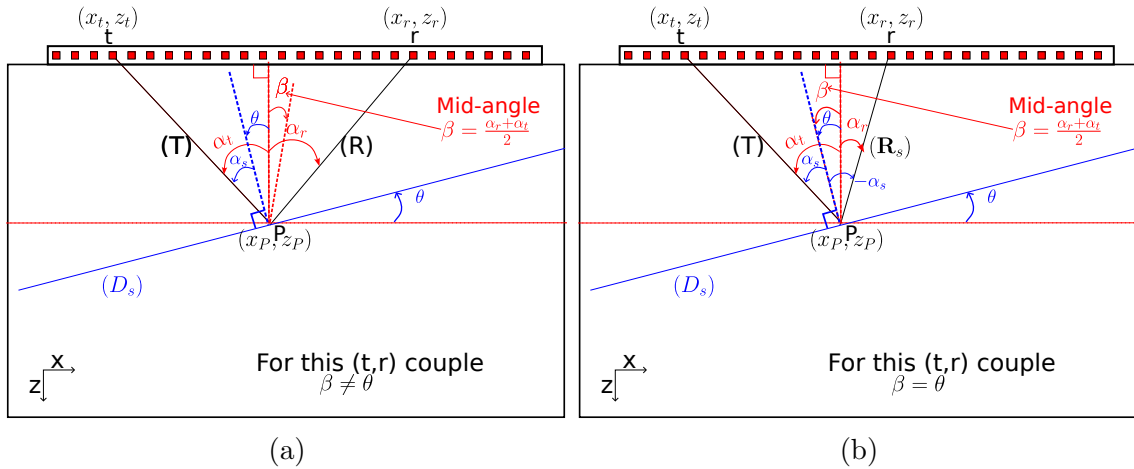


Figure 5.2: Geometric illustration of specular reflection in a homogeneous medium with a θ -tilted reflector. The ultrasound ray from t (T) hits the reflector at P . Element r is recording all backscattered signals from the medium. In panel (a) elements t and r are chosen to satisfy laws of specular reflection. In panel (b) chosen receiving element r does not satisfy specular reflection.

We define α_t as the angle between the incident ray (T) and the normal of the probe and α_r the angle between the reflected ultrasound ray travelling from point P to element r (R) and the normal of the probe. If we choose (t, r) satisfying physical laws of specular reflection as in Figure 5.2b, we can write:

$$\begin{aligned} \alpha_s &= \alpha_t - \theta \\ -\alpha_s &= \alpha_r - \theta, \end{aligned} \quad (5.2)$$

yielding

$$\alpha_r + \alpha_t - 2\theta = 0. \quad (5.3)$$

Angular values α_r and α_t can be obtained from positions of t , r , and P using

following trigonometric relationships (Figure 5.2):

$$(r, t) \hookrightarrow (\alpha_r, \alpha_t)$$

$$\alpha_r(P) = \arctan\left(\frac{x_P - x_r}{z_P - z_r}\right) ; \quad \alpha_t(P) = \arctan\left(\frac{x_P - x_t}{z_P - z_t}\right) \quad (5.4)$$

For the rest of the chapter, the dependency of α_t and α_r to P is omitted but the reader must bear in mind that α_r and α_t depend on the pixel as given in equation (5.4).

Let us identify β as the transmit-receive mid-angle ($\beta = \frac{\alpha_r + \alpha_t}{2}$). Then, equation (5.3) is equivalent to:

$$\beta - \theta = 0. \quad (5.5)$$

This means that when the transmit-receive mid-angle at point P equals the specular orientation θ of the object passing through P , the received back-scattered energy maximizes the specular energy reflected by the object. Therefore, we see as expected that the choice of the transmit-receiver pair that maximizes the back-scattered energy of a specular reflector depends on the specular orientation. If the pair (t, r) does not satisfy the equation (5.5), then the transmit-receive mid-angle is different from θ (depicted in Figure 5.2a).

The above relationship creates a signature specific to specular reflections. Rodriguez-Molares et al.[5] illustrated this signature with theoretical developments using the above equations and the image source principle. Following their work, in the next section, we will illustrate this signature in a set of simulations made with the MUST toolbox [12].

5.2.2 The specular signature

We simulated a linear array of 128 elements with a spacing of 300 μm . A synthetic transmit aperture sequence (SA) [13; 14] is simulated as acquisition scheme: each of the 128 elements of the probe emits a Gaussian-windowed tone burst with a central frequency of 2.5 MHz and all the elements of the probe record the back-scattered signals. This gives 128×128 back-scattered RF signals. We used 4 different configurations for the simulations. In all configuration, a fluid medium is considered with speed of sound $V_0 = 1540 \text{ m/s}$.

- In the first configuration, we simulated a single diffuse point scatterer at position (0,20) mm in a homogeneous medium to illustrate diffuse reflection (Figure 5.3a).
- In the second configuration, we generated a pseudo random distribution of scatterers such that the mean distance between a scatterer and its nearest neighbor is approximately half of the wavelength at 2.5 MHz (300 μm). This configuration simulates speckle noise (Figure 5.3b).
- In the third configuration, a plane reflector tilted by $\theta = 10^\circ$ passes through the pixel at coordinates (0,20) mm(Figure 5.3c).
- In the last configuration (see panel 5.3d), we generated a pseudo random distribution of scatterers as in the second configuration and added a plane reflector tilted by $\theta = 10^\circ$ passing through the pixel at coordinates (0,20) mm (as in the third configuration).

Specular signature of specular objects. The delay corresponding to a wave-front emitted by the t^{th} element of the probe to the scatterer P of coordinates (x_P, z_P) recorded by the probe at r^{th} element is given by:

$$\tau_{t,r}(P) = \frac{1}{V_0} \left(\sqrt{(x_P - x_t)^2 + (z_P - z_t)^2} + \sqrt{(x_P - x_r)^2 + (z_P - z_r)^2} \right), \quad (5.6)$$

the first square root term of the equation is the incident travel time and the second term is the reflection travel time. $\tau_{t,r}(P)$ is called in the literature the two-way travel time.

Recorded signals from each focal point of the medium (corresponding to a pixel in the reconstructed image) can be written as a matrix of RF signals consisting of 128 rows and 128 columns where each element of the matrix represents the back-scattered signal from pixel P recorded by r^{th} element of the probe when the t^{th} element is emitting $S(\tau_{t,r}(P), r, t)$. In Figure 5.3, we show the matrix of delayed signals for a focal point at (0,20) mm for each configuration.

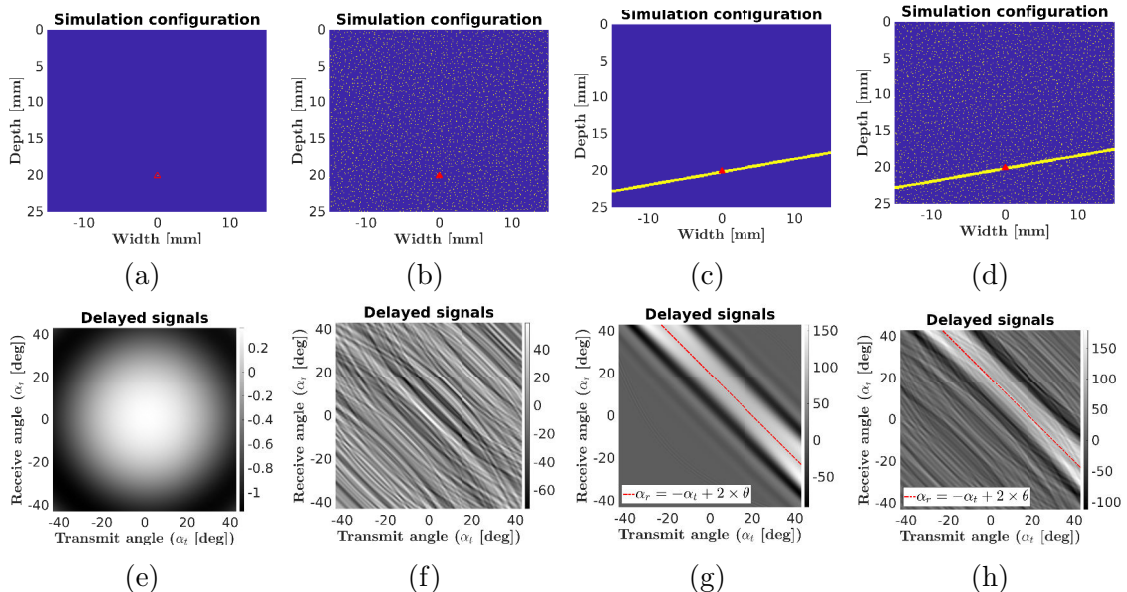


Figure 5.3: Illustration of received signal from a pixel located at depth (0,20)mm (red triangle in the top row images) for all different configuration. The top row images (panels (a), (b), (c) and (d)) are the simulation configuration and the bottom row images (panels (e), (f), (g) and (h)) are the corresponding delayed received signals with respect to receive and transmit angle. Panel (a): an homogeneous medium containing a single point-scatterer located at (0,20) mm. Panel (b): a medium where numerous point scatterers are randomly distributed such that the mean distance between two scatterers is 300 μm . Panel (c): a homogeneous medium containing a specular interface with orientation $\theta = 10^\circ$ passing through (0, 20) mm. Panel (d): a homogeneous medium containing numerous point scatterers as in (b) and a specular interface as in (c). The red lines in panels (e) and (h) are the plot of the specular reflection equation 5.3 for $\theta = 10^\circ$.

For the first configuration (panel a of Figure 5.3), we see that the corresponding delayed signals (panel e) are uniformly distributed across all couples of elements. The radial decay of the signal's intensity from the center of the matrix ($\alpha_r = 0, \alpha_t = 0$)

is due to the directivity of the simulated receiving elements and the radial decay of the propagation of a spherical wave as expected.

In the second configuration (panel b of Figure 5.3), the map of delayed signals at the focal point shows some randomness. This is principally due to the scattering of randomly located scatterers. This is what we refer as speckle noise.

We can see in the two last configurations that the corresponding received signals (panels 5.3g and 5.3h) present strong amplitude and similarity for couples satisfying equation (5.3) (e.g. in the direction $\alpha_r = -\alpha_t + 2 \times \theta$ corresponding to the red line in the panels). This is what we refer as specular signature. Specular beamforming consists of extracting this specular information out of speckle noise.

The results obtained in this simulation are the same as those of [5].

The specular transform. When performing DAS beamforming, an estimation of the reflectivity of pixel P is given by averaging delayed received signals. Classically, to avoid off-axis signal and account for element directivity, an apodisation window is chosen by setting a fixed transmit and receive f-number. The principle of apodisation based on f-number is given in the first Chapter and details can be found in [1]. Recall that fixing the f-number is equivalent to fixing the angular receive and transmit aperture. The relationship between f-number ($f_{\#}$) and angular aperture Δ_{α} is given by:

$$f_{\#} = \frac{1}{2 \tan\left(\frac{\Delta_{\alpha}}{2}\right)}. \quad (5.7)$$

For illustration, we choose here a receive and transmit f-number of 1 which corresponds to a fix receive aperture of $\pm 22^\circ$. Therefore, the pixel value in a DAS image with these parameters is the average of delayed signals inside a square box centered around 0° and of width $\Delta_{\alpha} = 44^\circ$. A diffuse point scatterer isotropically reflects the incident energy. We can see in Figure 5.4, where a blue box represents the averaging region, that most of the back-scattered energy is concentrated inside the blue box. Hence, the average of signals inside the box is a good estimate of the point reflectivity.

For the case of a specular reflector, the back-scattered energy is no longer concentrated around the lateral position of the pixel, therefore the energy is not confined around a receive and transmit angle of 0° . Depending on the orientation of the specular interface, the box will only include part of the back-scattered energy along with destructive interferences. We illustrate this in Figure 5.5 for a specular object with different orientations θ : 0, 10 and 20° . For the interface parallel to the probe surface (see panel 5.5a), the averaging region includes an important part of the specular reflection but also an important part of speckle noise. Although we are adding both constructive and destructive interference, averaging inside the blue box gives a good estimate of the specular reflection due to the fact that specular signal is much stronger than speckle noise. Hence, DAS images gives good estimate of flat interfaces. However, with increasing absolute specular orientation, the part of specular reflection will decrease (see panels 5.5b and 5.5c) and speckle contribution will increase. If the orientation of the specular object is greater than the maximum mid-angle of the transmit-receive aperture (blue box), then DAS will not detect the specular reflection. Therefore, DAS will fail to give a fair estimate of the reflectivity of pixel belonging to specular tilted objects.

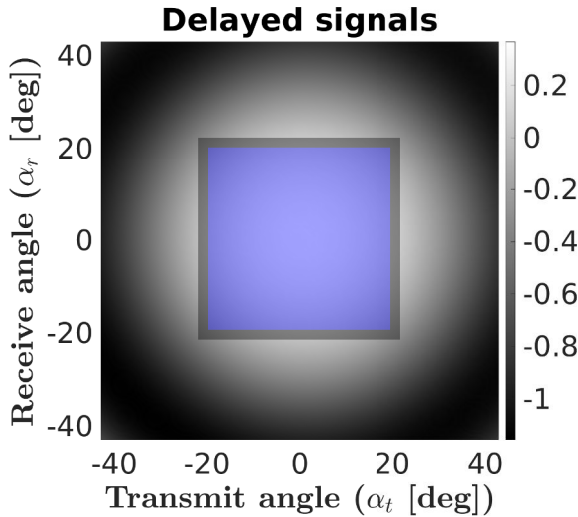


Figure 5.4: Delayed received signals from a diffuse point scatterer. The blue box centered around $(\alpha_t = \alpha_r = 0)$ is the region of interest that DAS beamforming uses to average the signal to estimate the reflectivity of the pixel. This box represents a f-number of 1.

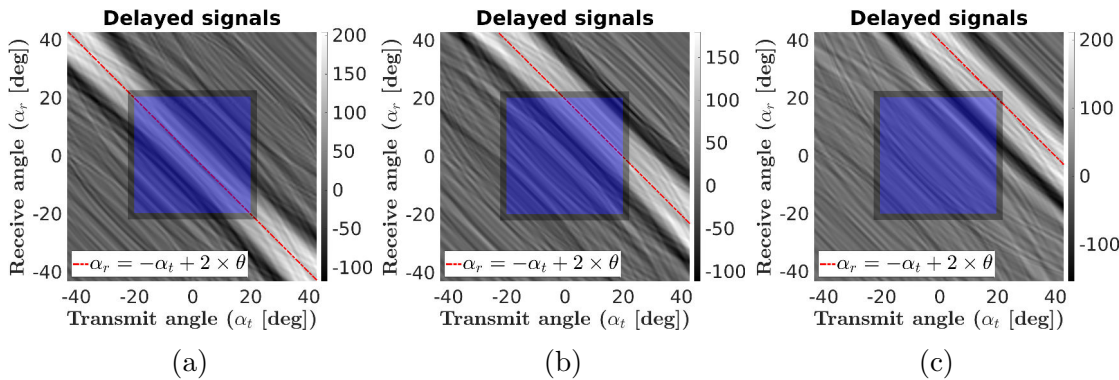


Figure 5.5: Delayed received signals from a point lying on a specular interface with different orientations. Panel (a): $\theta = 0^\circ$, panel (b): $\theta = 10^\circ$, and panel (c): $\theta = 20^\circ$. The blue box centered around $(\alpha_t = 0, \alpha_r = 0)$ is the region of interest that DAS beamforming uses to average the signal to estimate the reflectivity of the pixel. This box represents a f-number of 1.

To overcome this poor estimation of tilted specular reflector, Rodriguez-Molares et al [5] proposed to transform the matrix of delayed signals into a so-called specular domain. The principle arises from Equation (5.5) which says that all transmitter-receiver pairs that share the same mid-angle β will maximize the back-scattered energy from a specular interface of orientation β . Therefore, signals of transceiver pairs associated with a common mid-angle (β) are summed to give a single signal. This means summing along each anti-diagonal of the matrix of delayed signals. Doing so, specular reflections add up constructively and diffuse scattering interferes randomly. The specular transform is a 1D signal that represents the contribution of all specular orientation:

$$f(\beta; P) = \sum_{t=1}^{N_t} \mathbf{S}(\tau_{t,r}(P), \alpha_r, \alpha_t) \Big|_{\frac{\alpha_r+\alpha_t}{2}=\beta} \quad (5.8)$$

This way of summing signals of transmit-receiver pairs that correspond to the same transmit-receive mid-angle has been used previously in compute ultrasound tomography in echo mode using Common Mid-Angle appellation by [15] to accurately predict the distribution of the phase of the received signals and provide an estimate of the speed-of-sound map of the medium.

Note that in this notation and in the rest of the chapter, we changed variables of \mathbf{S} from (τ, r, t) to $(\tau, \alpha_r, \alpha_t)$.

Figure 5.6 shows the specular transform of received signals in configurations of panels 5.3b and 5.3d.

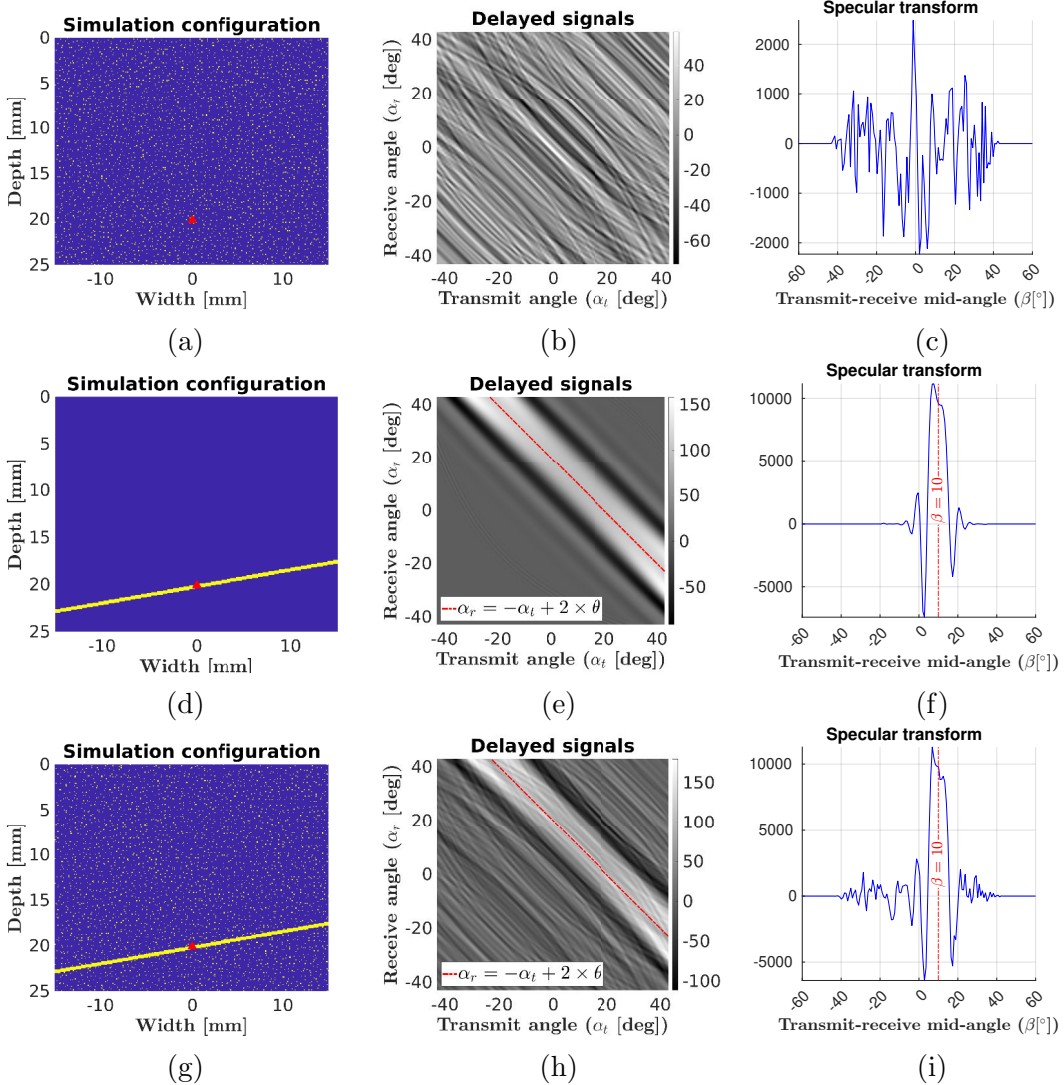


Figure 5.6: Illustration of the specular transform for a pixel located at (0,20)mm in different configurations. The first row correspond to the pure speckle configuration, the second row corresponds to pure specular interface with orientation 10° and the last row correspond to a configuration of specular interface surrounded with multiple point scatterers.

In a purely diffuse scattering regime, the specular transform presents randomness (see panel 5.6c). In the presence of a θ -oriented interface, the specular transform is maximum when the mid-angle $\beta = \theta$ and has a specific shape (see panel 5.6i and 5.6f). The red line in panels 5.6e and 5.6h corresponds to equation (5.3)

and the red line in panels 5.6f and 5.6i corresponds to equation (5.5) where the orientation of the specular object θ equals 10° .

The specular transform contains information on: (i) the presence of a specular reflector (specularity) and (ii) the orientation of the reflector (specular orientation). Specularity can be obtained by observing the shape of the specular transform. For example, if the shape of the received signal is random as in Figure 5.6c we can deduce that the reflector is not specular. On the other hand, if the shape is similar to the specular transform of a specular reflector we can deduce that the reflector is a specular object. The transmit-receive mid-angle β that maximizes the specular energy is the specular orientation θ . For example this mid-angle is around 10° in panel 5.6i.

If we derive a model of a specular transform parting from the known emitted signal, we can formulate the estimation of the specularity as a situation where we have to maximize the energy of a known signal (specular reflection) drown into unwanted random signal (speckle noise).

5.2.3 Model of specular transform

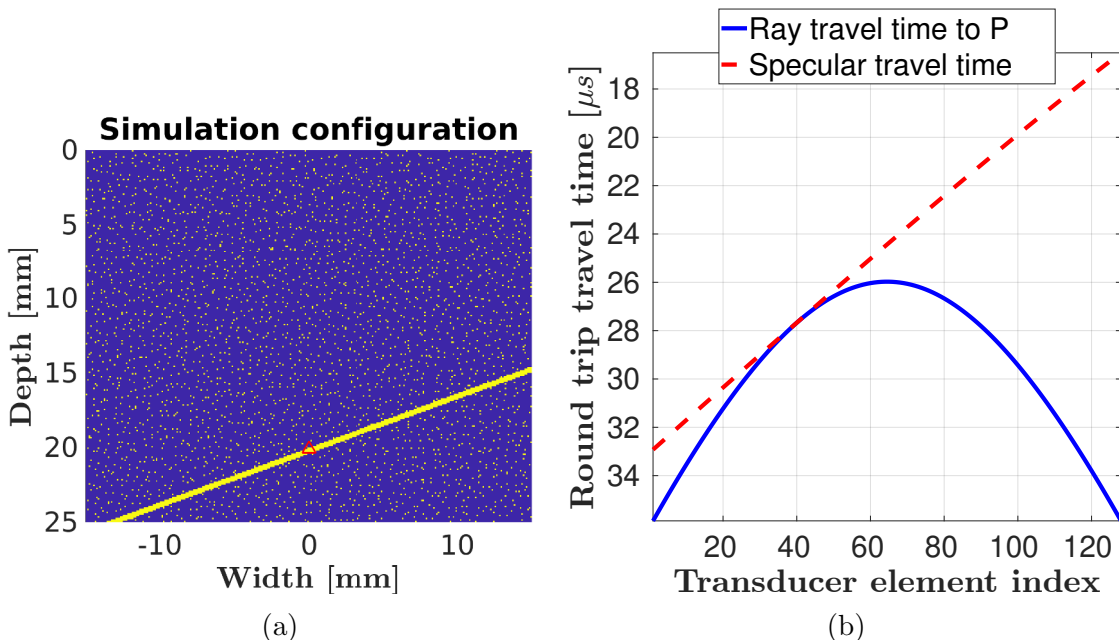


Figure 5.7: Comparison of specular and diffuse travel time for a point lying on a tilted planar interface. Panel (a) is the simulation configuration and the red triangle corresponds to the point for which travel times are computed. In panel (b), the computed specular travel time is plotted as a red dashed-line and the diffuse ray travel time is plotted in plain blue line. To compute these values the transmitting element is also the receiving element ($t=r$).

In Figure 5.7, we show the specular and the diffuse travel time for a point belonging to a specular interface (the red pixel in panel 5.7a). We suppose that the transmitting element is the receiving elements ($t=r$). The red dashed line corresponds to the two-way travel time of the specular reflection at point $P=(0,20)$ mm and the blue plain curve corresponds to the two-way travel time if we consider the

pixel as a point scatterer (this correspond to the diffuse travel time given by equation 5.6). We can see that for a diffuse travel time, the first arrival of the wavefront is recorded at the center of the probe (the blue plain curve is symmetrical and minimal around transducer elements 64 and 65). However, if we suppose a specular travel time with specular orientation $\theta = 20^\circ$, the first arrival of the specular wavefront is recorded at the element closer to the specular interface (element 128 of the probe). The diffuse travel time equals the specular travel time for element number 40. At this element, the transmit-receive mid-angle β equals the specular orientation θ .

Parting from this observation, our problem can be formulated as follows: we want to derive a model that gives the signal contribution from an orientation β (that corresponds to the transmit-receive mid-angle) knowing that the specular object has an actual orientation of θ .

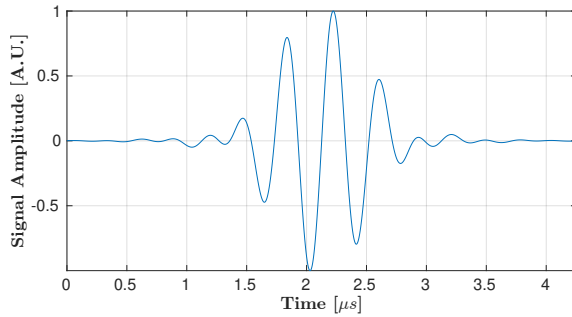


Figure 5.8: Emitted waveform $e(t)$ by elements of the probe.

A θ -oriented plane interface passes through $P(x_P, z_P)$ as in figure 5.2. Signal emitted by the element t is a Gaussian tone burst shown in the Figure 5.8 and denoted $e(t)$. When reaching the interface (D_s), the signal is reflected then recorded by element r . Since the reflection at (D_s) is specular, there exists a unique point $Q \equiv (x_Q, z_Q)$ belonging to the interface, such that the pairs of transmit and receive angles at point Q ($\alpha_t(Q), \alpha_r(Q)$) given by the equation (5.4) will satisfy the law of specular reflection (equation (5.3)). This point Q is called the mirror point of the couple (t, r) (see Figure 5.9).

We introduce the two way specular travel time as the time it takes to record with element r a wavefront emitted by the element t and reflected by a specular interface passing through P . This time corresponds to the diffuse two-way travel time (equation (5.6)) applied to mirror point Q : $\tau_{t,r}(Q)$ (blue plain ray path in Figure 5.9). In ray theory, the first specular reflection will be recorded at this time. The ray travel time to point P is given by $\tau_{t,r}(P)$ (black dashed ray path in Figure 5.9). Hence, the specular contribution at point P is given by the value of the shifted echo: $e(\tau_{t,r}(P) - \tau_{t,r}(Q))$.

According to Snell's law of reflection, the transmit-receive mid-angle of the pair (t, r) at the mirror point Q equals the specular orientation θ . Therefore all pairs of (t, r) that share the same mid-angle θ will also share the same mirror point Q . Therefore, to take into account the multiplicity of the transmission, we can derive a model of specular signal at point P as:

$$h(\beta; P, \theta) = \sum_{t=1}^{N_t} \sum_{r=1}^{N_r} e(\tau_{t,r}(P) - \tau_{t,r}(Q)), \quad (5.9)$$

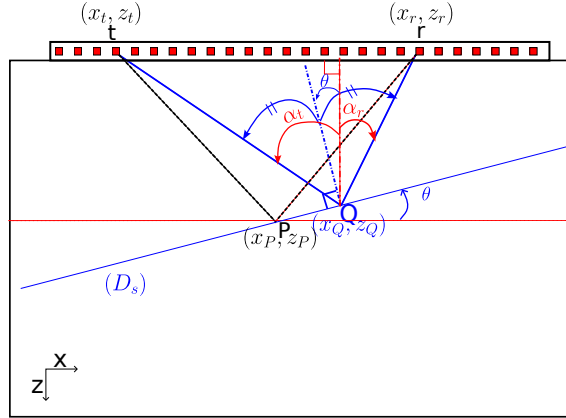


Figure 5.9: Geometric representation of specular reflection. Signal is emitted by t and received by element r . A θ -oriented interface is passing through pixel P . The corresponding mirror Point of this interface is Q and at this point $\alpha_r(Q) + \alpha_t(Q) - 2\theta = 0$. Ray path that follows Snell-Descartes law is in blue plain line whereas ray path is plotted in black dashed line.

in this notation Q means mirror point and depends on the position of the transmitting t and receiving r elements. This dependency is voluntary omitted for simplicity of notation.

Authors of [5] derived a model of specular transform for a homogeneous medium based on the image source principle. In this chapter the principle of mirror point is used to explain the development of the model but it is strictly equivalent to the image source principle.

Determination of the mirror point Q . Parting from laws of specular reflection, we know that the mirror point Q belongs to the interface (D_s) and it also satisfies equation (5.3). This gives:

$$\begin{cases} z_Q = -\tan(\theta)(x_Q - x_P) + z_P \\ \alpha_r(Q) = 2\theta - \alpha_t(Q) \end{cases}$$

Using the trigonometric relationship of equation (5.4), we solve this system of two equations to find (x_Q, z_Q) :

$$x_Q(t, r) = \frac{b(1 - a^2)(x_r + x_t) + 2a(x_r x_t - b^2)}{(a^2 + 1)[2b + a(x_r + x_t)]}, \quad (5.10)$$

$$z_Q(t, r) = ax_Q(t, r) + b,$$

with $a = -\tan(\theta)$ and $b = z_P + x_P \tan(\theta)$.

This analytical determination of the mirror point will allow us to get specular travel time from equation (5.6) and thus compute the specular model given by the expression in (5.9) for any specular orientation.

In figure 5.10, the specular model h is shown for different values of specular orientation θ : $-20, -10, 0, 10$ and 20 degrees.

The maximum amplitude of the specular model is highest when the assumed specular interface is parallel to the probe ($\theta = 0^\circ$) and decreases as θ increases.

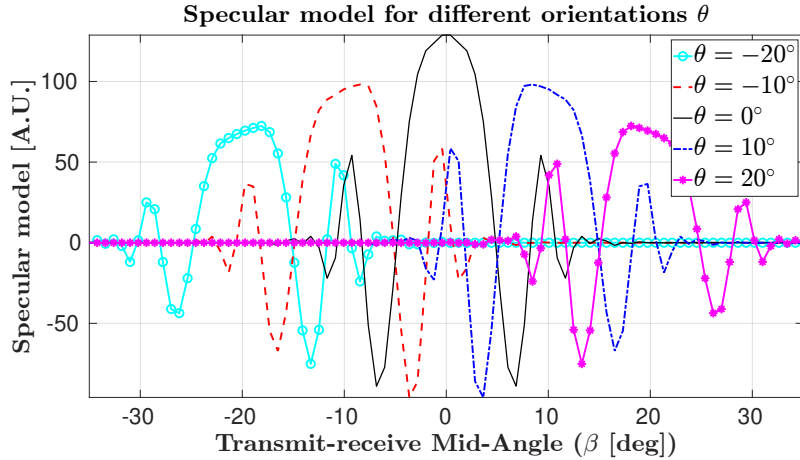


Figure 5.10: Models $h(\beta; P)$ of specular signal computed with equation (5.9). The model is shown for 5 different specular orientations: from -20 to $+20^\circ$.

The slight asymmetry observed, depending on the sign of the specular orientation, is a result of the reduction in the number of transmitter-receiver pairs as the angle moves away from 0 degrees.

We observed in Figure 5.3 that delayed received signals exhibit symmetry concerning the Snell-Descartes equation (5.3). Specifically, for all pairs sharing the same mid-angle β , identical specular reflections are recorded. Since our focus is solely on the shape of the specular signal, we can derive a simplified model $h_0(\beta; P)$ by considering only one transmit-receiver pair for each β . We can limit our consideration along the axis $\alpha_r = \alpha_t$, corresponding to the diagonal of delayed signals in Figure 5.3.:

$$h_0(\beta; P, \theta) = \sum_{t=1}^{N_t} e(\tau_{t,t}(P) - \tau_{t,t}(Q)). \quad (5.11)$$

In figure 5.11, the simplified specular model h_0 is shown for different values of specular orientation θ : -20 , -10 , 0 , 10 and 20 degrees.

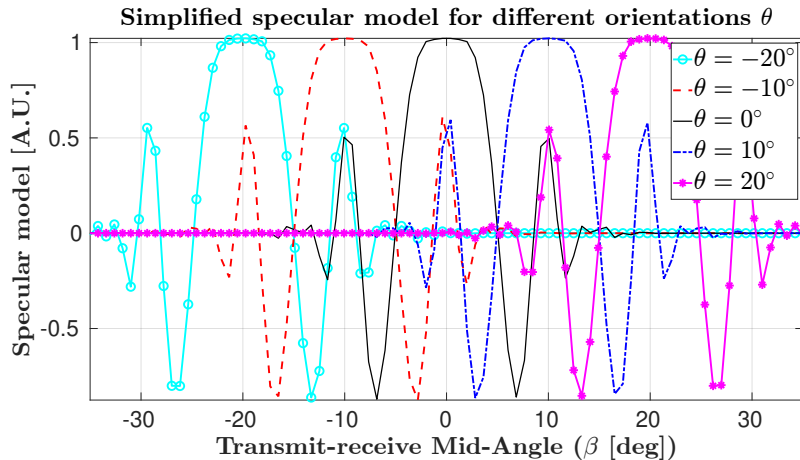


Figure 5.11: Models of specular signal computed with equation (5.11). The model is shown for 5 different specular orientations: from -20 to $+20^\circ$.

The expected signal maintains the same shape and reaches its maximum at the specular orientation θ . Notably, the model remains invariant with respect to θ .

Therefore, the specular model of a θ -oriented interface $h_0(\beta; P, \theta)$, can be approximated by the specular model of a flat interface $h_0(\beta; P, 0)$ translated by θ .

In the presence of a specular reflection, the known shape will be embedded in unwanted speckle. The objective is now to maximize the ratio of specular to unwanted speckle energy.

5.2.4 Model-based characterization of the specular reflection

Following Rodriguez-Molares et al., we define the specularity of a pixel as the probability that there is a specular interface passing through this pixel. To estimate the specularity of P , we calculate the normalized correlation between the model of specular signal $h_0(\beta; P, \theta = 0)$ and the specular transform of the received signals $f(\beta; P)$.

$$\chi(\theta; P) = \frac{\int_{\beta} f(\beta; P) \cdot h_0(\beta - \theta; P, 0) d\beta}{\sqrt{\int_{\beta} f(\beta; P)^2 d\beta \cdot \int_{\beta} h_0(\beta; P, 0)^2 d\beta}} \quad (5.12)$$

Normalizing the cross-correlation by the maximum correlation of a perfect match will give values between 0 and 1. A value close to 1 means that the two signals are nearly the same and a value close to 0 means the two signals are very different.

In Figure 5.12, we plot the normalized cross-correlation $\chi(\theta; P)$ for a pixel P when there is a specular reflector surrounded by numerous point scatterers (first column of the figure) and for a case where there is only speckle noise (second column of the figure).

We observe that even in the presence of speckle noise, the signal received from a specular interface is highly correlated with the specular model of a flat interface: we obtain a maximal value close to 1 (0.9) for $\theta = 20^\circ$ (panel 5.12d). However when there is only speckle noise, the specular signal is poorly correlated to the specular model of a flat interface (panel 5.12e). Hence, one can deduce from these correlation results, an estimate of the specularity Ψ of a pixel as the maximum of the normalized cross-correlation $\chi(\theta; P)$.

$$\Psi(P) = \max(\|\chi(\theta; P)\|). \quad (5.13)$$

The angle that maximises this correlation gives an estimate of the orientation $\tilde{\Theta}(P)$ of the specular interface passing through P :

$$\tilde{\Theta}(P) = \arg \max_{\theta} (\|\chi(\theta; P)\|). \quad (5.14)$$

Finally, we obtain a specularity map Ψ which is an estimation of the specularity of objects inside the imaging medium and a map of orientation $\tilde{\Theta}$ which is an estimation of the orientation of the specular objects. In figure 5.13 we show the specularity maps and the corresponding specular orientation of each pixel of a medium containing an interface with orientation $\theta = 20^\circ$ surrounded by randomly distributed diffuse scatterers.

Panel b of Figure 5.13 is the specularity map and panel c is the estimation of specular orientation for pixels with specularity greater than 0.5. We can see that the specularity is maximal and close to 1 at the object location (panel 5.13b) and low at other locations. The estimation of orientation of pixels having a good specularity (greater than 0.5) gives value close to 20° (see Figure 5.13c).

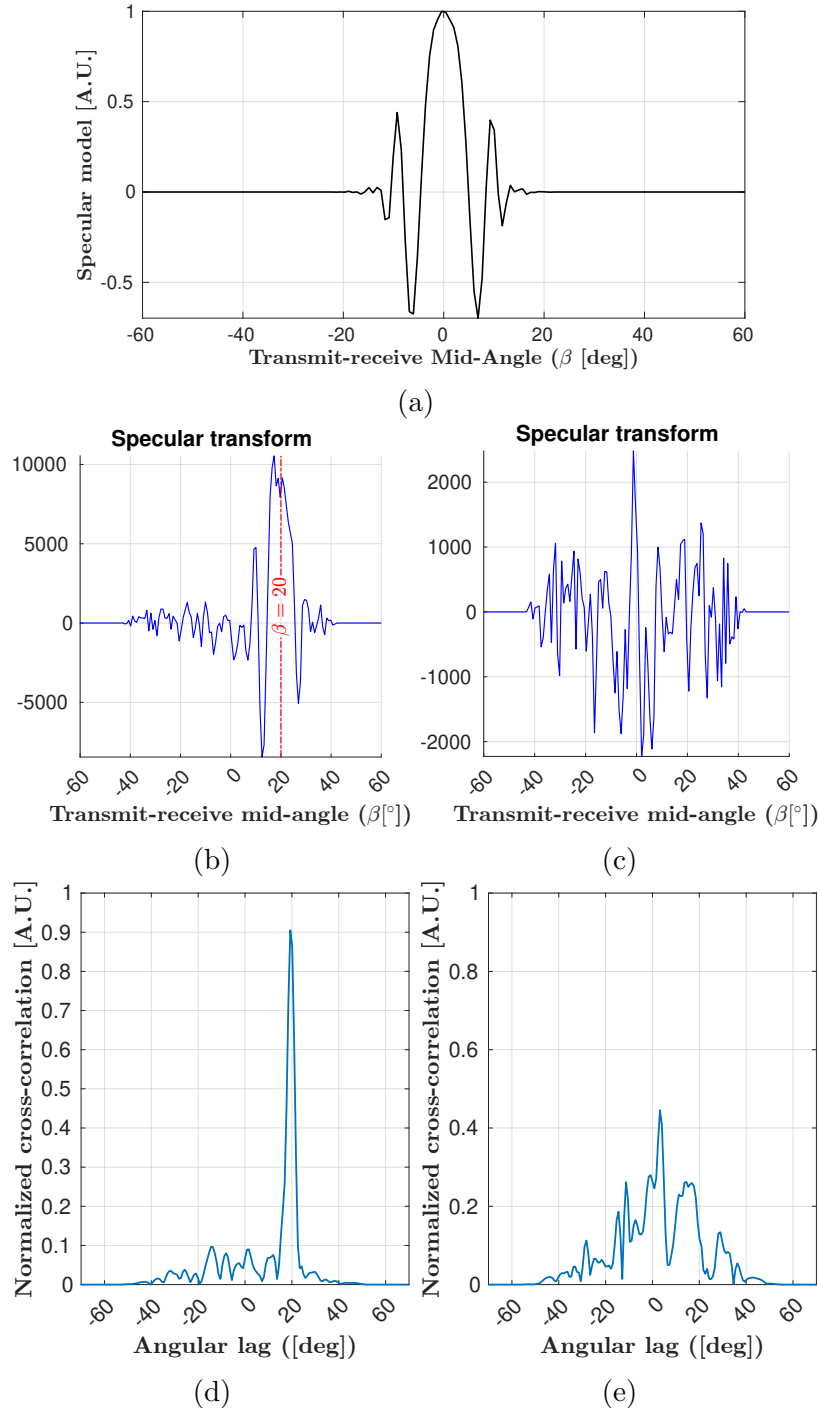


Figure 5.12: Illustration of correlation between a model of specular transform $h_0(\beta; P; \theta = 0)$ (panel (a)) and received specular transform $f(\beta; P)$. The first column (panels (b) and (d)) corresponds to a configuration of a specular interface surrounded by numerous point scatterers and second (panels (b) and (d)) corresponds to a configuration of randomly distributed point scatterers.

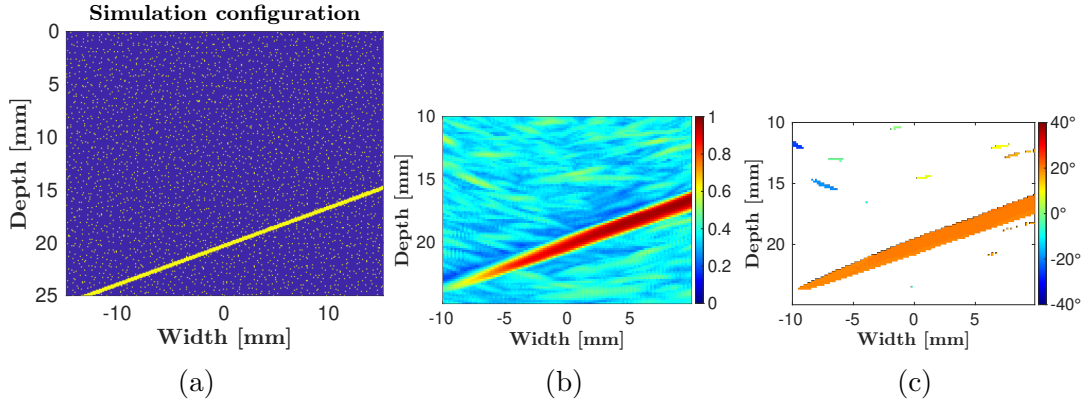


Figure 5.13: Characterization of specularity of a medium containing a specular interface with orientation $\theta = 10^\circ$ drown into randomly distributed point scatterers. Panel (a) shows the medium configuration, panel (b) is the map of estimated specularity obtained equation 5.13 and panel (c) is the map of estimated specular orientation computed with equation 5.14 for pixels that have a specularity above 0.5.

5.3 Refraction-corrected specular beamforming for multi-layered media

All of the development above supposed a homogeneous medium in which waves propagate in straight line. However we saw in previous chapters that the impedance of bone-tissue is at least twice higher than that of soft tissues. Therefore, the hypothesis of straight ray path is not a good approximation for the case of bone. In this section, we will illustrate refraction and specular reflection for a two-layers medium. We give a generalized model-based characterization of curved specular interfaces. In the scope of this chapter, we neglect lens of the probe.

5.3.1 Geometrical considerations

Refraction. We suppose a medium with two layers: a layer of cutaneous tissue on top of a layer of bone tissue. The interface between the two layers can be approximated by a parabola with parameters a_0, a_1, a_2 :

$$(D_e) : z = a_0 + a_1 x + a_2 x^2, \quad (5.15)$$

where x and z are along the axes defined in Figure 5.14. V_1 and V_2 are the propagating wave-speed inside cutaneous tissue and cortical bone respectively. We define α_t (respectively α_r) as the angle of the incident ray parting (respectively the reflected ray) from element t (respectively received at element r) of the probe and γ_t (respectively γ_r) as the angle of the ray arriving at (respectively parting from) point P inside cortical bone (see Figure 5.14).

We define incident point J as the point of the interface through which the incident ray passes and incident point K as the point of the interface through which the

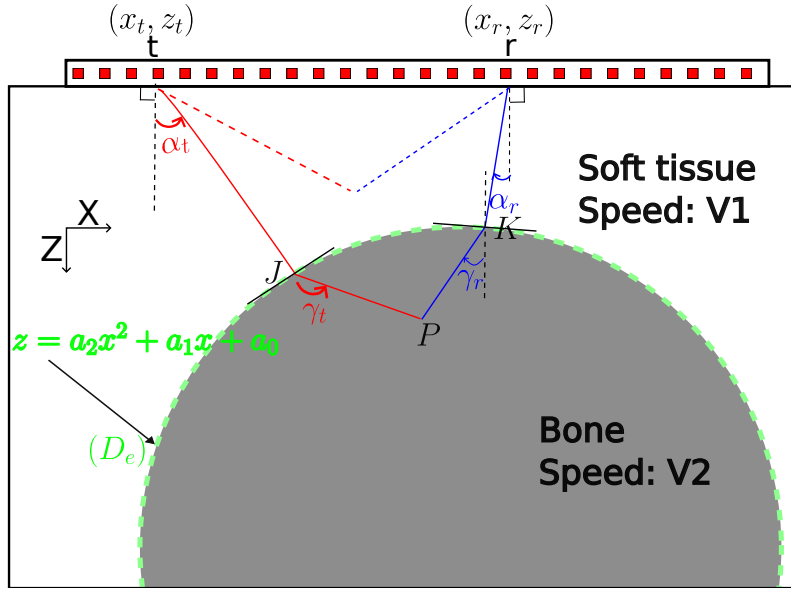


Figure 5.14: Illustration of refraction at the external interface of cortical bone

reflected ray passes. Using these points above angles are given by:

$$\begin{cases} \alpha_t = \arctan\left(\frac{x_J - x_t}{z_J - z_t}\right) \\ \gamma_t = \arctan\left(\frac{x_P - x_J}{z_P - z_J}\right) \\ \alpha_r = \arctan\left(\frac{x_K - x_r}{z_K - z_r}\right) \\ \gamma_r = \arctan\left(\frac{x_P - x_K}{z_P - z_K}\right) \end{cases} \quad (5.16)$$

According to Snell-Descartes law of refraction for the transmitted ray from t to P :

$$\frac{\sin(\alpha_t(P) + \arctan(2a_2x_J + a_1))}{V_1} = \frac{\sin(\gamma_t(P) + \arctan(2a_2x_J + a_1))}{V_2}. \quad (5.17)$$

The reflected ray from P to r follows the same laws:

$$\frac{\sin(\alpha_r(P) + \arctan(2a_2x_K + a_1))}{V_1} = \frac{\sin(\gamma_r(P) + \arctan(2a_2x_K + a_1))}{V_2}, \quad (5.18)$$

where the arctan terms are the local orientations of the external interface at points J and K .

Let us denote $\sigma_{t,r}(P)$ as the two-way travel time that considers refraction between layers. Hence, we obtain the relationship:

$$\sigma_{t,r}(P) = \frac{\sqrt{(x_J - x_t)^2 + (z_J - z_t)^2} + \sqrt{(x_K - x_r)^2 + (z_K - z_r)^2}}{V_1} + \frac{\sqrt{(x_P - x_J)^2 + (z_P - z_J)^2} + \sqrt{(x_P - x_K)^2 + (z_P - z_K)^2}}{V_2}. \quad (5.19)$$

Point J depends on both emitting element t and focal point P , point K depends on both receiving element r and focal point P . After angular transformation using equation (5.16), J and K can be obtained by finding the points that satisfy equations (5.17) and (5.18) respectively. If the external interface is planar, analytic

developments give solutions for point J and K . However, if the external interface is not planar, solving these equations is not trivial. In fact, if we develop the expression 5.18 or 5.18 , we find a non-polynomial equation. Solutions are found using numerical methods. We used MATLAB 2023a and its non-linear zero finding algorithm *fzero* Copyright 1984-2021 The MathWorks, Inc.

Specular reflection. Suppose that we have a curved reflector (D_i) inside the cortex as in Figure 5.15. The reflector can be approximated by a parabola with

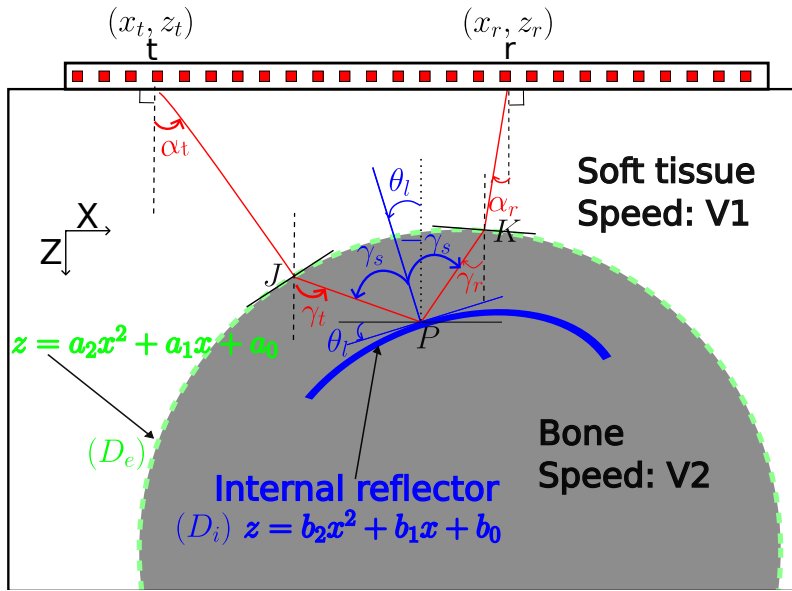


Figure 5.15: Illustration of specular reflection inside cortical bone

parameters b_0 , b_1 and b_2 :

$$(D_i) : z = b_0 + b_1x + b_2x^2 \quad (5.20)$$

We can apply the laws of specular reflection to a point P belonging to this interface. We can derive an equation similar to equation 5.3. This yields the same law:

$$\gamma_t + \gamma_r - 2\theta_l = 0, \quad (5.21)$$

where θ_l is the local orientation of the interface passing through focal point P and its value is given by $-\arctan(2b_2x_P + b_1)$.

5.3.2 The specular signature in presence of refraction

We consider a two-layer medium with the inclusion of different reflectors as in section 5.2 in the second layer. (see Figure 5.16 panel (a) to (d)).

We performed simulations with SimSonic software ([16]). A synthetic aperture imaging sequence with an array transducer (central frequency 2.5 MHz and a 3 dB bandwidth of 80%) of 128 elements of size 245 μm and spaced 300 μm was simulated. The first layer is a homogeneous fluid medium with water speed of sound $V_1=1540$ m/s and the second layer is a homogeneous elastic medium with longitudinal wave-speed of sound $V_2 = 3500$ m/s mimicking bone matrix. The simulated probe is immersed inside the first layer and the interface between two layers is at 10 mm depth from the probe surface. For this configuration 4 scenarios were considered:

- a scenario to illustrate diffuse scattering, a diffuse point scatterer is centered and placed at 20 mm depth, (Panel 5.16a)
- a scenario to illustrate pure speckle noise, numerous point scatterers are randomly placed in the second layer, (Panel 5.16b)
- a scenario to illustrate pure specular scattering, a specular object with an orientation $\theta = 10^\circ$ is placed at 20 mm depth, (Panel 5.16c)
- a scenario to illustrate specular scattering drown into speckle noise, a specular object with an orientation $\theta = 10^\circ$ is placed at 20 mm depth and is surrounded by numerous point scatterers randomly distributed, (Panel 5.16d)

Recorded signals from a focal point $P = (0, 20)$ mm for each configuration are shown in Figure 5.16 from panel e to panel h. The same signature are observed as for an homogeneous medium (Figure 5.3). Signature of diffuse point scatterer in panel e is less marked in this case. In fact, the wavelength inside second layer is 1.4 mm instead of 0.6 mm giving a point scatterer more smaller compared to the wavelength. Therefore, the diffusion strength is smaller. Due to this small size of the scatterer, some numerical artifacts appear as we can see in the diagonal of the image in figure 5.16e.

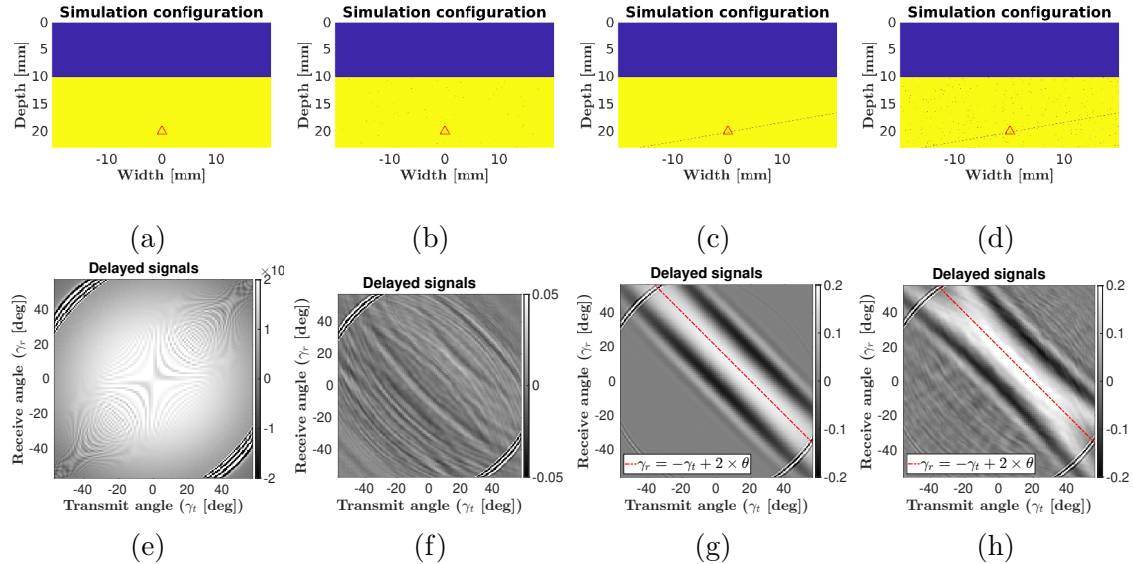


Figure 5.16: Delayed received signals from a pixel located at depth (0,20)mm inside the second layer (red triangle in the top row images) for all different configurations. The first layer is water with speed of sound of 1540 m/s and the second layer is bone matrix with speed of sound 3500 m/s. The top row images (panels (a), (b), (c) and (d)) are the simulation configuration as in Figure 5.3 and the bottom row images (panels (e), (f), (g) and (h)) are the corresponding delayed received signals with respect to receive and transmit angle at the pixel. The red lines in panels (e) and (h) are the plot of the specular reflection equation 5.21 for $\theta = 10^\circ$

In panels e to h of Figure 5.16, we observe in the upper left and lower right corners of the image the unwanted reflections from the external interface at 10 mm.

These are the signals that follow an equivalent propagation path but do not originate from the wanted direction. These are contribution of secondary lobes and they can be eliminated with an appropriate f-number.

Apart from these artifacts and noise, we obtain the same specular patterns as in section 5.2.

The specular transform From the above results, specular signature does not change when refraction is considered appropriately. We can therefore use the specular transform by considering the receive and transmit angle at the pixel (γ_t, γ_r) . Hence, the same transformation as in equation 5.8 translates the received signals in the specular domain through :

$$f(\beta; P) = \sum_{t=1}^{N_t} \mathbf{S}(\sigma_{t,r}(P), \gamma_r, \gamma_t) |_{\frac{\gamma_r + \gamma_t}{2} = \beta} \quad (5.22)$$

Figure 5.17 shows the specular transform of received signal for the configurations with pure speckle noise and for specular reflection with speckle noise.

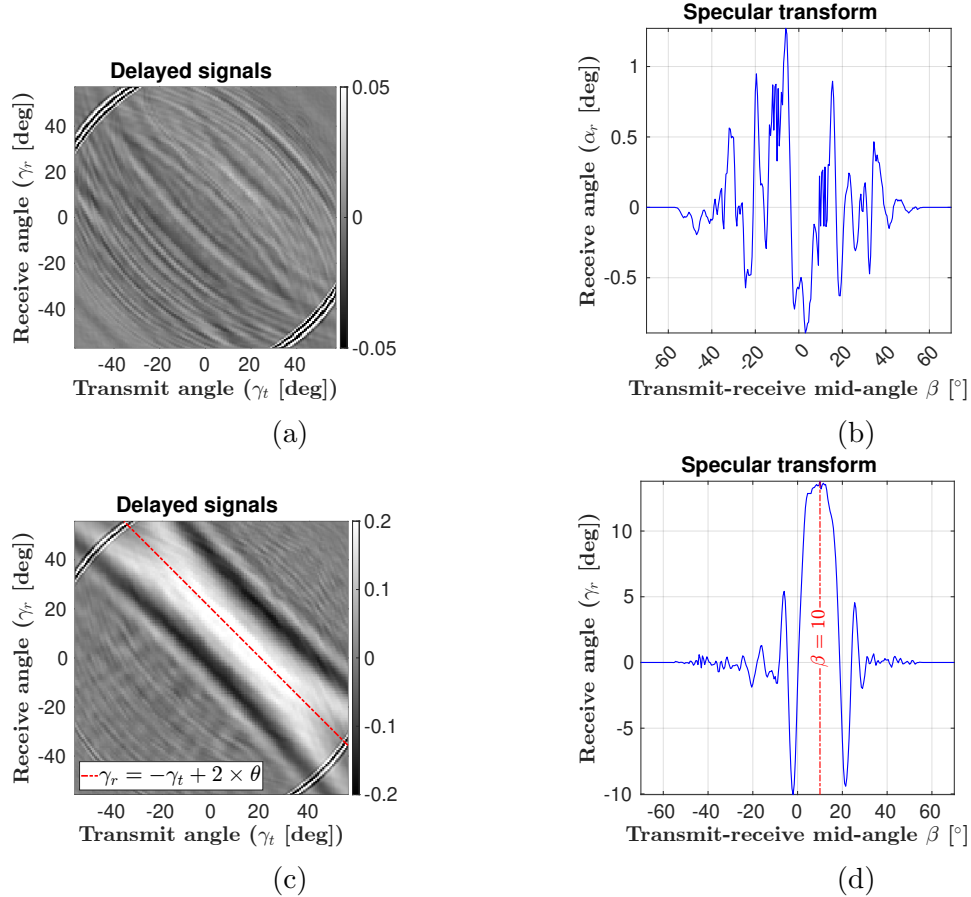


Figure 5.17: Illustration of the specular transform for a pixel located at (0,20)mm. First column: delayed received signals and last column corresponds to specular transforms. First row: pure speckle configuration (panels (a) and (b)), the second row: a specular interface surrounded by numerous point scatterers (panels (c) and (d)).

As expected, specular transform exhibits the specular signature and the same shapes as in Figure 5.6 . After transformation, speckle noise is random (panel b)

and specular reflection exhibits a certain shape specific to specular reflector (panel d). Remark that the specular transform of panel 5.17d is wider than the specular transform of panel 5.6i. In fact, the full angular width at half maximum is around 7° for Figure 5.6g and around 15° for Figure 5.17d which corresponds to an increase of a factor of 2. This is due to the fact that the wavelength inside second layer (1.4 mm) is around twice higher than the wavelength inside water (600 μm).

5.3.3 Model of specular transform

We derive a model of specular transform for a two-layered medium. Same principle as in section 5.2.3 is applied in the second layer but the travel time must consider refraction.

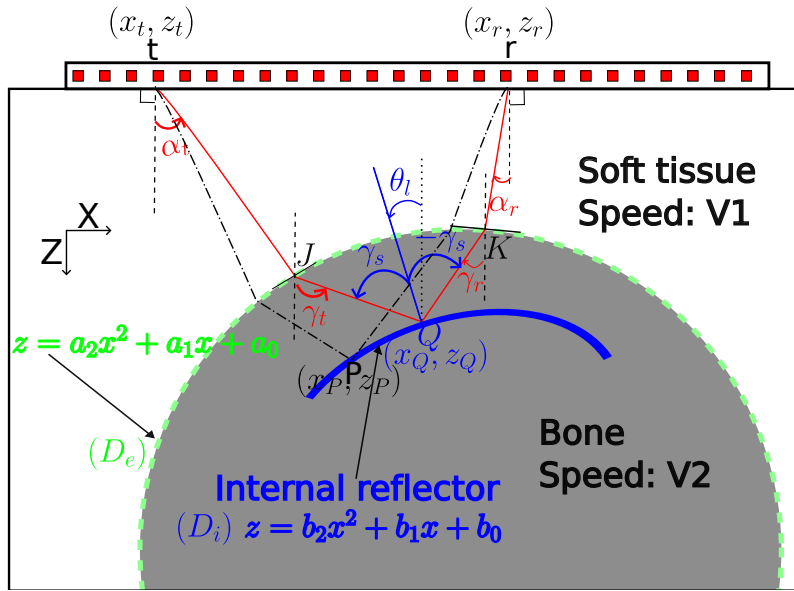


Figure 5.18: Geometrical illustration of specular reflection at the internal interface of the bone.

The reflector inside the second layer (D_i) is a parabola given by equation (5.20) (Figure 5.15). The parameter b_2 determines the curvature of the reflector. A positive value means a convex reflector and a negative value means a concave reflector. For the scope of this study, we will ignore concave reflectors and suppose that b_2 is always positive. If $b_2 = 0$, then we have a planar reflector with orientation $-\arctan(b_1)$. For non-null values of b_2 , the curvature of the reflector increases with b_2 . For this reason, b_2 is called the parameter of curvature and b_1 the parameter of local orientation.

When reaching the interface between the layers (D_e), part of the incident ray is reflected and another part is refracted inside bone cortex. At the reach of the specular reflector, the refracted ray is reflected and element r records the back scattered signal after another refraction (black dashed ray path in figure 5.18). Therefore, it exists a unique point $Q \equiv (x_Q, z_Q)$ belonging to interface D_i such that the transmit and receive angles at point Q will satisfy the law of specular reflection and specular refraction given in equations (5.18), (5.17) and (5.21) (blue plain ray path in figure 5.18). This point noted Q is the mirror point (Figure 5.18).

Hence, the specular travel time that considers refraction is given to delay equation 5.19 applied to point Q : $\sigma_{t,r}(Q)$. Recording of specular reflection will start at

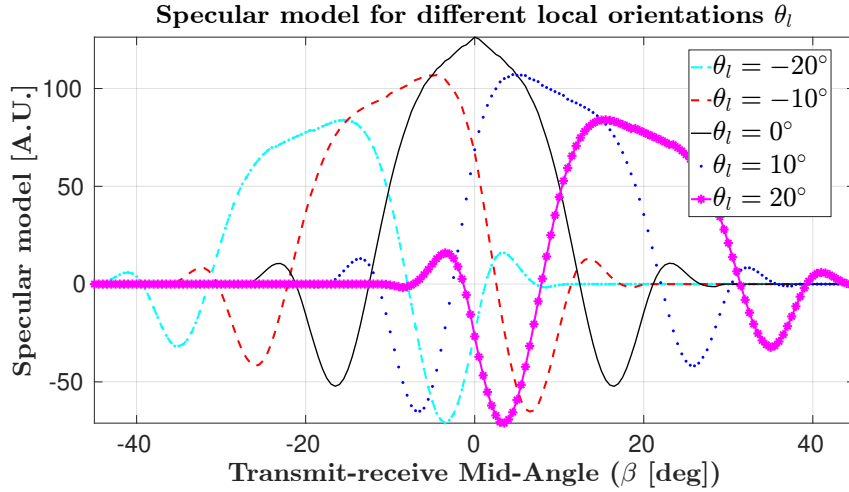


Figure 5.19: Specular model for a specular interface inside the cortex with fixed curvature ($b_2 = 30 \text{ mm}^{-2}$) and varying local orientations θ_l . Parabolic parameters of the external interface are: $a_0 = 10 \text{ mm}$, $a_1 = 0$, $a_2 = 30 \text{ mm}^{-2}$

this time. The ray travel time is given by $\sigma_{t,r}(P)$. In the same manner as in section 5.2, the specular contribution at point P is the shifted echo $e(\sigma_{t,r}(P) - \sigma_{t,r}(Q))$ and the model can thus be obtained by applying equation 5.9. Note that the travel time now also depends on the parameters of the external interface (a_0, a_1, a_2) .

Determination of the mirror point Q Parting from laws of specular reflection and refraction, we know that the coordinates of mirror point Q depends on the parameters of the external interface D_e , on the coordinates of the transmitting and receiving elements and it also belongs to the reflector D_i . Mathematically, this means:

$$\left\{ \begin{array}{l} z_Q = b_0 + b_1 x_Q + b_2 x_Q^2 \\ \gamma_r(Q) = -2 \arctan(2b_2 x_Q + b_1) - \gamma_t(Q) \\ \frac{\sin(\alpha_t(P) + \arctan(2a_2 x_J + a_1))}{V_1} = \frac{\sin(\gamma_t(P) + \arctan(2a_2 x_J + a_1))}{V_2} \\ \frac{\sin(\alpha_r(P) + \arctan(2a_2 x_K + a_1))}{V_1} = \frac{\sin(\gamma_r(P) + \arctan(2a_2 x_K + a_1))}{V_2}, \end{array} \right. \quad (5.23)$$

where J and K are the incidents point of the incident and reflected wave respectively. Using the trigonometric relationship in equation 5.16, we can replace angles and solve the system 5.23. For the case of a single homogeneous medium and a planar reflector, analytical development of the coordinates of a mirror point could be found. In this present case of a multi-layer medium with curved specular interfaces, analytical developments are difficult to obtain. Hence, we use numerical computation to obtain x_Q and z_Q . We solved the non-linear system 5.23 using MATLAB 2023a and its non-linear zero finding algorithm *fzero* Copyright 1984-2021 The MathWorks, Inc.

In figure 5.19, we plot the specular model obtained after computation of mirror points for 5 different local orientations ranging from -20° to $+20^\circ$ and fixed curvature parameter b_2 ($b_2 = 10 \text{ m}^{-1}$). As expected, this model is similar to the model obtained for a planar interface in Figure 5.10.

In Figure 5.20, the local orientation of the specular interface is fixed to 10° , and specular model are plotted for 4 different curvatures of the reflector: $b_2 = 0 \text{ m}^{-1}$, $b_2 = 20 \text{ m}^{-1}$, $b_2 = 40 \text{ m}^{-1}$ and $b_2 = 60 \text{ m}^{-1}$. We remark that the spreading of

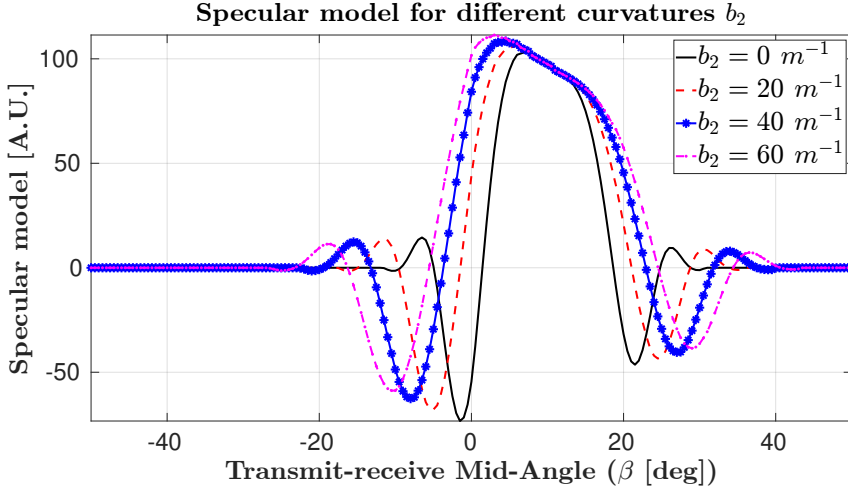


Figure 5.20: Specular model for a specular interface inside the cortex with fixed local orientation ($\theta_l = 10^\circ$) and varying curvatures b_2 . Parabolic parameters of the external interface are: $a_0 = 10$ mm, $a_1 = 0$, $a_2 = 30$ mm $^{-2}$.

specular model increases with curvature but the center is the same. Therefore the parameter of curvature b_2 changes the shape of the model. Hence, the simplified specular model h_0 for a curved reflector of curvature b_2 and orientation b_1 passing through point P is given by:

$$h_0(\beta; P, b_1, b_2) = \sum_{t=1}^{N_t} e(\sigma_{t,t}(P) - \sigma_{t,t}(Q)). \quad (5.24)$$

The parameter b_1 only shifts the simplified model but does not change its shape and b_2 changes the shape of the model. Hence, h is invariant to b_1 . We can then implement the matched filter by using the normalized cross-correlation between the model $h_0(\beta; P, b_1 = 0, b_2)$ and $f(\beta; P)$.

$$\chi(\theta_l; P, b_2) = \frac{\int_\beta f(\beta; P) \cdot h_0(\beta; P, 0, b_2) d\beta}{\sqrt{\int_\beta f(\beta; P)^2 d\beta \cdot \int_\beta h_0(\beta; P, 0, b_2)^2 d\beta}}. \quad (5.25)$$

We deduce the specularity by taking the maximum correlation :

$$\Psi(P) = \max(\|\chi(\theta_l; P, b_2)\|). \quad (5.26)$$

This maximum corresponds to a local orientation $\tilde{\theta}_l$ and a curvature \tilde{b}_2 given by :

$$[\tilde{b}_2, \tilde{\Theta}_l](P) = \arg \max_{b_2, \theta_l} (\|\chi(\theta_l; P, b_2)\|). \quad (5.27)$$

Estimate of the orientation parameter \tilde{b}_1 can be deduced from the relationship $\tan \tilde{\theta}_l = -(2\tilde{b}_2 x_P + \tilde{b}_1)$.

Similarly, one can generalize this procedure for a medium where the number of layers is above 2 and for other interfaces governed by higher degree polynomial. We then can get for any pixel, specular transform and a specular model that considers refraction. This allows to proceed to the model-based characterization of all reflections of the medium.

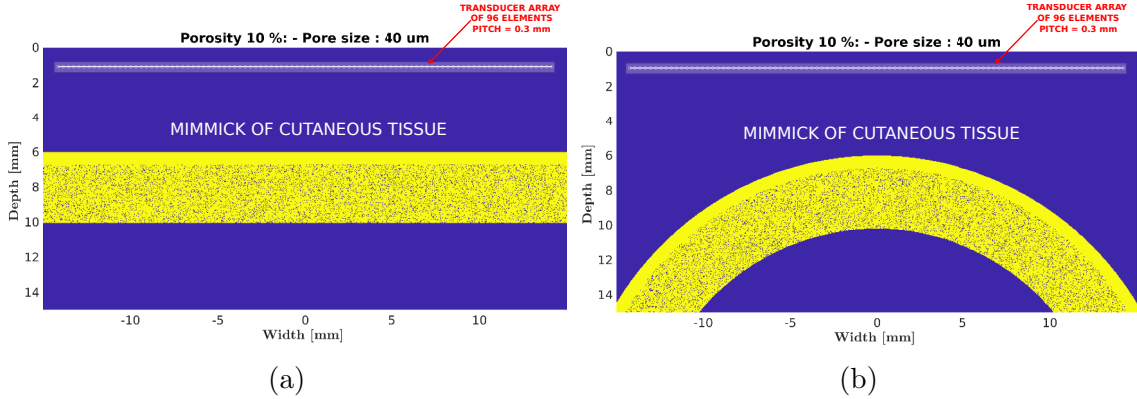


Figure 5.21: Three-layers model used for simulations: two layers mimicking cutaneous tissue (blue) and one layer mimicking cortical bone tissue (yellow). Different geometries were generated: flat interfaces (left) and curved interfaces (right). The simulated probe is a linear array of 96 elements with a pitch of $300 \mu\text{m}$

5.4 The impact of pore scattering on the contrast of specular images: a 2D simulation study

In sections 5.2 and 5.3, we explained how the laws of specular reflection and refraction can be utilized to classify and characterize reflections in a medium. These methods provide information on the specularity of the reflection and the orientation of the interface. While we illustrated the method with simulations of simple configurations where the specular interface is a needle-like object inserted into a homogeneous medium, these simulations are not representative of ultrasound imaging of cortical bone. In ultrasound imaging of cortical bone using delay-and-sum beamforming, pore scattering is known to be detrimental to image quality [17].

In this section, we investigate the influence of pore scattering on the contrast of specular images of the endosteal surface. We generate datasets that simulate various levels of diffuse scattering in a multi-layered media (Figure 5.21a). We explore both planar and curved geometries of bone surfaces. To simplify the study and emphasize the impact of pore size, we assume that all pores in each microstructure have the same diameter.

The technique outlined in section 5.3 is employed on the generated datasets, and the resulting images are compared with DAS images.

5.4.1 Materials & methods

Simulation of the ultrasound imaging sequence. We employed an elastic slab model to simulate the bone layer, incorporating randomly distributed pores with fixed diameters. Three pore diameters ($10, 30$, and $50 \mu\text{m}$) were considered, each with three porosity levels (6% , 10% , and 14%) representing low, medium, and high porosity, respectively. For each diameter-porosity combination, microstructures were generated with both flat and curved bone interface geometries (Figure 5.21b).

The bone layer was enveloped by a soft tissue-mimicking layer. For the soft tissue mimicking layers, a compressional wave speed of 1540 m/s was employed. Regarding the mineralized matrix within the cortical bone-mimicking layer, the compressional

and shear wave speeds used in the simulations were 3500 m/s and 1800 m/s, respectively. The material within the pores was assumed to be the same as that in the soft tissue layer. We utilized the SimSonic open software [16] to generate ultrasound signals. To prevent reflections at the boundaries of the simulation domain, a Perfectly Matched Layer (PML) boundary condition with a thickness of 3 mm (approximately 5 wavelengths in soft tissues) was implemented.

Within the cortical bone mimicking layer, we modeled frequency-independent absorption within the bone matrix, with an absorption coefficient of 19.0 dB/cm at 2.5 MHz. The simulations were conducted with a grid size of 10 μm , and the corresponding time step was determined to maintain a constant value of CFL=0.99.

We simulated the same probe as used in experimental measurements, consisting of a linear array with 96 elements and a pitch of 300 μm . A synthetic transmit aperture sequence was simulated. Each of the 96 elements emitted a Gaussian-windowed tone burst with a central frequency of 2.5 MHz (3dB bandwidth=1.33 MHz, Figure 5.22), and all the elements recorded the back-scattered signals. This resulted in a 96×96 matrix of back-scattered RF signals \mathbf{S} .

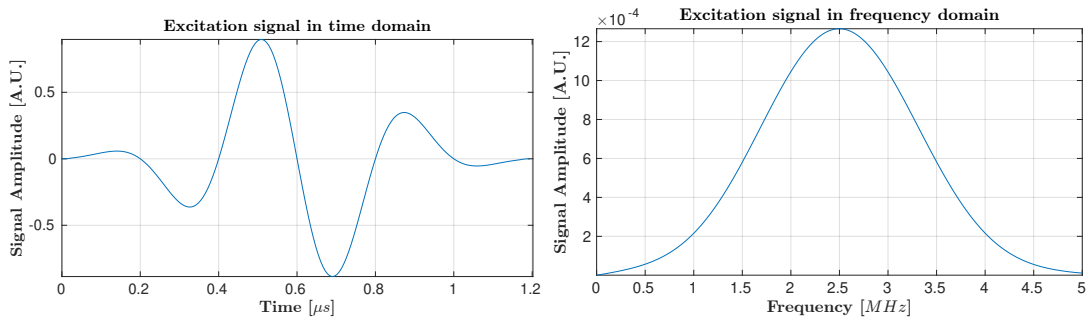


Figure 5.22: Emitted tone burst in temporal domain (left) and in frequency domain (right). Gaussian-windowed tone burst with a central frequency of 2.5 MHz and a 3 dB bandwidth of 1.33 MHz,

Beamforming with delay-and-sum algorithm. DAS algorithm is used with a constant receive f-number of 0.5. This corresponds to a constant angular aperture at the transducer's elements of 45 degrees. Let's denote the corresponding lateral receive aperture Δ_r . Lateral aperture will depend on depth of the pixel. The relationship between lateral aperture and pixel's depth is obtained with f-number $f_\#$ definition ([1]):

$$f_\# = \frac{z_P}{\Delta_r(P)}$$

The delays used to produce a low-resolution image are obtained from equation 5.19.

When a wavefront hits a diffuse point scatterer, it is isotropically radiated in all directions. Hence, the DAS consists of performing, for each transmission, a weighted sum over the delayed received signal. The window used here is a hann window centered on the lateral position of the pixel and its size is fixed by the receive f-number. Equation 5.28 gives the signal ($d(t; P)$) obtained at focal point P

with transmitting element number t :

$$d(t; P) = \sum_{r=1}^{N_r} w(r; P) \cdot \mathbf{S}(\sigma_{t,r}(P), r, t), \quad (5.28)$$

where $w(r; P)$ denotes the apodisation window used for pixel P (combination of f-number and hann window centered at lateral pixel coordinates).

$$w(r; P) = \begin{cases} \cos^2\left(\frac{\pi(x_r - x_P)}{\Delta_r}\right), & \text{if } |x_r - x_P| \leq \Delta_r(P) \\ 0, & \text{if } |x_r - x_P| > \Delta_r(P) \end{cases}$$

This transformation applied to all pixels leads to 96 low resolution images which are coherently summed to get one high resolution image. A DAS image is then obtained with :

$$I_{DAS}(P) = \frac{1}{N_t} \sum_{t=1}^{N_t} w(t; P) \cdot d(t; P). \quad (5.29)$$

Beamforming with specular algorithm. The specular algorithm exploits the specularity of the reflection. It produces three outputs: (1) a specularity map Ψ that is the probability to find a specular structure at each pixel, (2) an orientation map $\tilde{\Theta}_l$ that is an estimate of the most likely orientation of the specular structure and (3) an image that highlights specular structures and reduces speckle which we refer as specular beamformed image. The specular beamformed image is a weighted sum of specular-transformed signals $f(\beta; P)$. A hann window centered around the estimated specular orientation $\tilde{\Theta}_l$ is used. Value of the specularity of the pixel P is used to enhance specular structure and remove speckles, thus, the intensity of the specular beamformed signal denoted I_{SP} is given by:

$$I_{SP}(P) = \Psi(P) \cdot \sum_{\beta=\beta_{min}}^{\beta_{max}} w(\beta; \tilde{\Theta}_l(P)) \cdot f(\beta; P), \quad (5.30)$$

, where $w(\beta; \tilde{\Theta}_l(P))$ denotes the apodisation window used for pixel P (a hann window centered around $\tilde{\Theta}_l(P)$).

$$w(\beta; \tilde{\Theta}_l(P)) = \begin{cases} \cos^2(\beta - \tilde{\Theta}_l(P)), & \text{if } |\beta - \tilde{\Theta}_l(P)| \leq \eta \frac{\pi}{2} \\ 0, & \text{if } |\beta - \tilde{\Theta}_l(P)| > \eta \frac{\pi}{2} \end{cases},$$

here, η is introduced as the specular tolerance, ranging from 0 to 1. When $\eta = 0$, only the specular reflection from the orientation $\tilde{\Theta}_l$ is taken into account. As η increases, more specular signals with decreasing weights are considered and summed. For reconstruction, we used $\eta = 0.1$ for planar interfaces and $\eta = 0.25$ for curved interfaces.

$d(t; P)$ and $f(\beta; P)$ contain all scattering information of the pixel but in different basis. The argument of the DAS output, t and P , are respectively the position of the emitting element $(x_t, 0)$ and the position of the pixel P (x_P, z_P) . The depth of the pixel is used to fix the receive aperture. The lateral position of the pixel fixes the value of the apodisation window. If the receiver and the pixel have same or close lateral position, the weight is close to 1 and when receiver's lateral position

gets further away from the lateral position of the pixel, the smaller is its weight. Hence, the DAS operation can be seen as gathering information according to the lateral distance between receiving element r and pixel P . The specular transform $f(\beta; P)$ gathers information according to the angular shift between the probe surface and a specular structure passing through P . Therefore, the main difference between these two algorithms lies in the summation basis and the apodization window used. They become equivalent when a rectangular window is used for both algorithms, a null f-number (full receive aperture) is used for DAS and a 100% specular tolerance ($\eta = 1$) is used for specular beamforming.

Speed of sound estimation. To perform beamforming, it is crucial to calculate travel times, which, in turn, requires knowledge of the speed of sound. While the propagating wave-speed inside soft tissues is well-known, the porous nature of the cortical bone layer leads to variations in speed due to changes in porosity. Thus, each layer is reconstructed sequentially using a specific sound speed for each microstructure.

We employ the autofocus principle, as outlined in Chapter 2, which suggests that among images generated with different velocity values, the optimal image in terms of brightness and sharpness is obtained when the velocity is closest to the velocity of the medium [10]. By utilizing various brightness and sharpness metrics, as detailed in Chapter 2, we determine the propagating wave-speed in the cortical bone layer. In figure 5.23, the estimated speed values are reported for all configuration. In panel (a) we plot the speed values for configurations with flat bone surfaces and in panel (b) the values for configurations with curved bone surfaces.

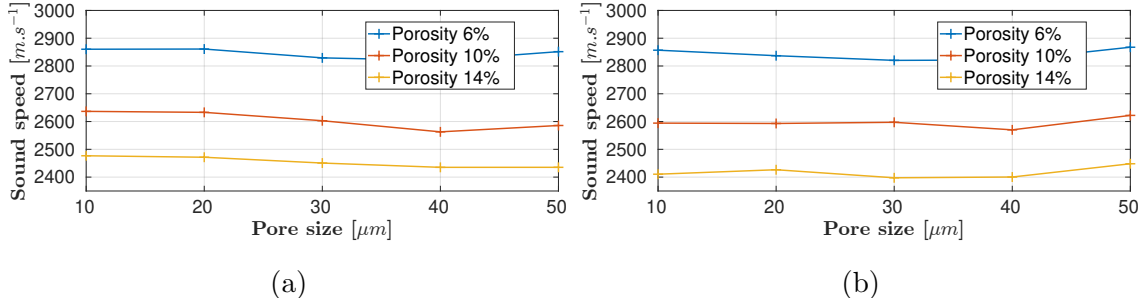


Figure 5.23: Speed of sound values in cortical bone obtained with autofocus approach for each cortical porosity and each individual pore size. Panel (a): flat bone interfaces. Panel (c): curved bone interfaces

As expected, the wave-speed values in cortical layer were found to decrease with respect to porosity. We also can remark that for a fixed porosity speed of sound slightly changes with pore size.

Endosteal interface visibility quantification. To evaluate the visibility of endosteal surface, we define the endosteal interface contrast (C_{EI}) as follows:

$$C_{EI} = \frac{\mu_E}{\mu_I}, \quad (5.31)$$

where μ_I and μ_E are respectively the average image intensities in the center of the cortex and at the endosteal interface. It is the same metric as the one defined in

Chapter 3 but adapted to these geometries. The regions of interest (ROI) used for the computation of μ_I and μ_E all had a lateral extent from -5 to $+5$ mm. They are defined in Figure 5.24, where: the red box is the endosteal interface ROI, it has a height of one wavelength inside the bone layer and the yellow box is the inner cortex ROI, it extends from 1 mm after periosteal interface region to 1 mm before endosteal region.

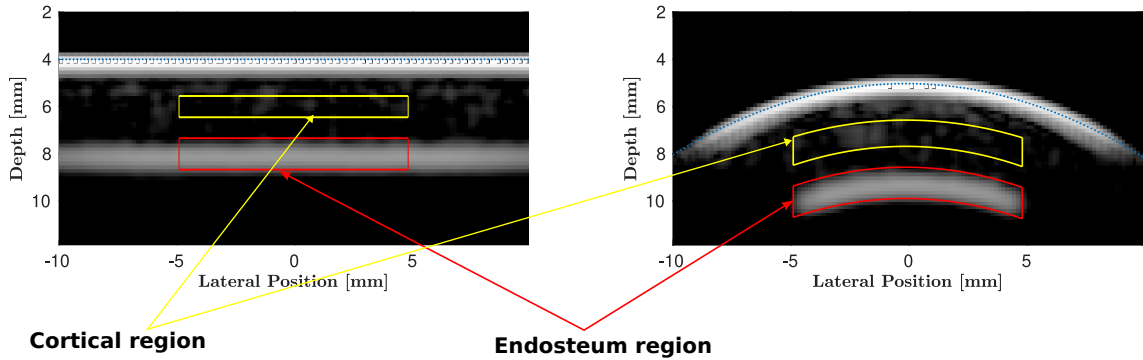


Figure 5.24: Region of interest to quantify endosteal interface visibility. Reconstructed images for a simulation configuration with flat interfaces (left) and configuration with curved interfaces (right). The yellow and red ROIs are used to evaluate inner bone cortex and endosteum contrasts, respectively.

C_{EI} evaluates how well the endosteal interface can be distinguished from the speckle inside the bone. On decibel scale, a positive value of C_{EI} means that endosteal interface is clearly visible while a negative value means that the endosteal interface is poorly visible.

5.4.2 Results

Parametric results on the presences of specular structures.

Planar interfaces. Figures 5.25, 5.26 and 5.27 display the maps of specularity Ψ and local orientation $\tilde{\theta}_l$ for configurations with planar bone interfaces and individual pore diameter of 10 , 30 and 50 μm respectively. The configurations corresponding to same microstructures but with curved interfaces are displayed in Figures 5.28, 5.29 and 5.30. In each figure, the panels of the top row (panel a, b and c) correspond to specularity map Ψ and panels of the bottom row (panels d, e and f) correspond to local orientation map $\tilde{\theta}_l$. Panels of first column (panels a and d) correspond to a cortical porosity of 6% , panels of second column (panels b and e) correspond to a cortical porosity of 10% and panels of third column (panels c and f) correspond to a cortical porosity of 14% .

We observe in Figure 5.25 probability values close to 1 (between 0.92 and 0.99) at depth around 5 mm and 9 mm. The apparent thickness of the first interface is higher than that of the second interface due to larger wavelength inside bone. The specularity of the endosteal interface slightly changes with porosity. Inside the cortex, lower specularity values are found (values are lower than 0.4). This yields a good contrast between interfaces and the cortex: $C_{EI} = 11 \text{ dB}$. Specular orientation found for relevant pixels (with specularity ≥ 0.5 , panel d, e and f) correspond to flat interfaces.

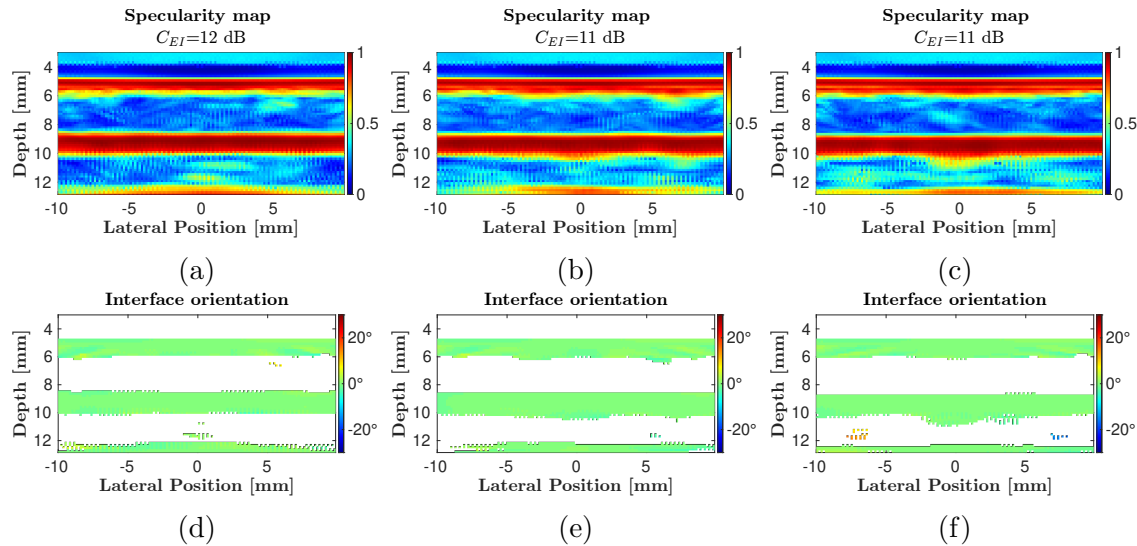


Figure 5.25: Specularity maps Ψ (top row images: panels a-c) and corresponding orientation maps $\tilde{\Theta}_l$ for pixel with specularity greater than 0.5 (bottom row images: panels d-f) for simulation configuration with flat bone interfaces. The diameter of the pore of the microstructure is $10 \mu\text{m}$. Panels a and d correspond to cortical porosity of 6%, panels b and e correspond to cortical porosity of 10% and panels c and f correspond to cortical porosity of 14%. Specular orientation is computed only for pixel with specularity greater than 0.5 with a scale ranging from -30 to 30° . In each map of specularity C_{EI} is calculated.

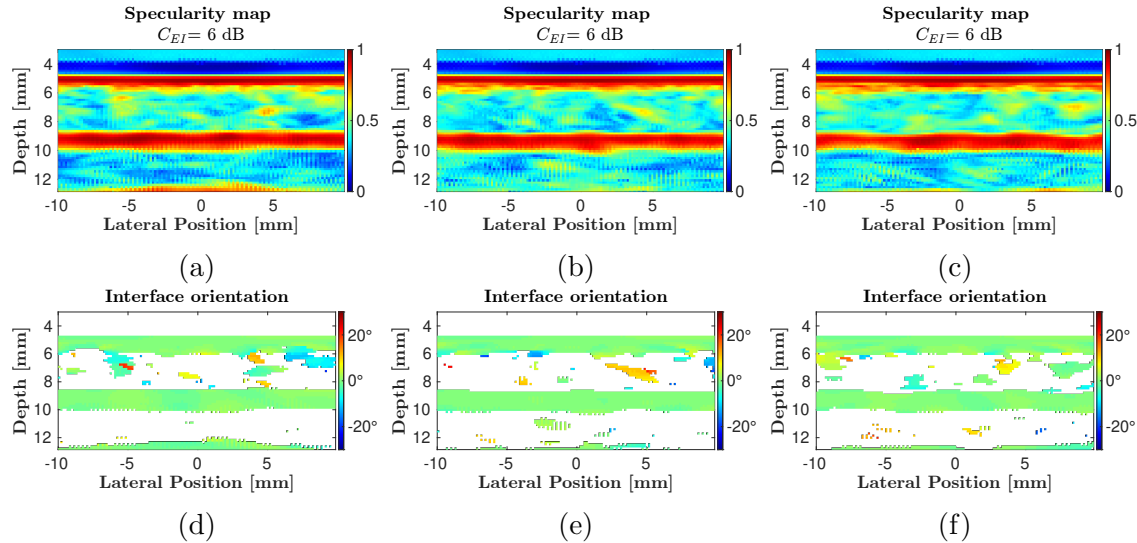


Figure 5.26: Same as figure 5.25 but the diameter of the pores is 30 μm .

In Figure 5.26 where individual pore diameter is 30 μm probability values at depth of bone interfaces are also close to 1 but lower than values found for configuration with pore diameter of 10 μm . Inside the cortex, some pixels have high specularity (values are greater than 0.5). This yields a lower contrast between interfaces and the endosteal surface: $C_{EI} = 6 \text{ dB}$. Specular orientation found for pixels of the interface correspond to flat interfaces but orientation for pixel inside the cortex are random.

For pore diameter of 50 μm (Figure 5.27), specularity of the internal interface

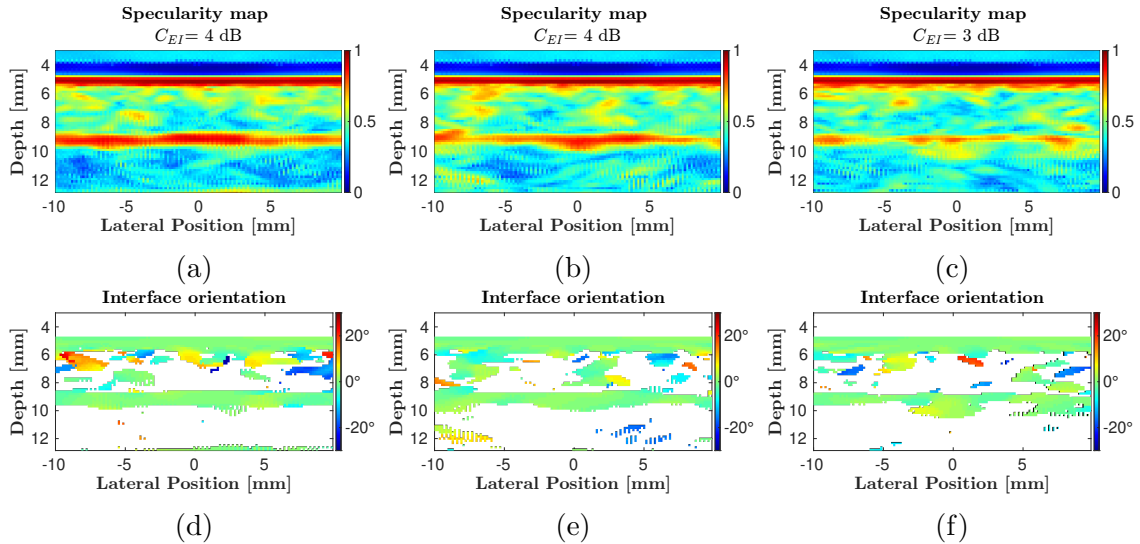


Figure 5.27: Same as figure 5.25 but the diameter of the pores is 50 μm .

decreases and number of "specular pixels" inside the cortex increases. Orientation of bone interface is accurately estimated and specular orientations inside the cortex are random. Visually, we observe a more pronounced decrease of the specularity of the endosteal interface with cortical porosity.

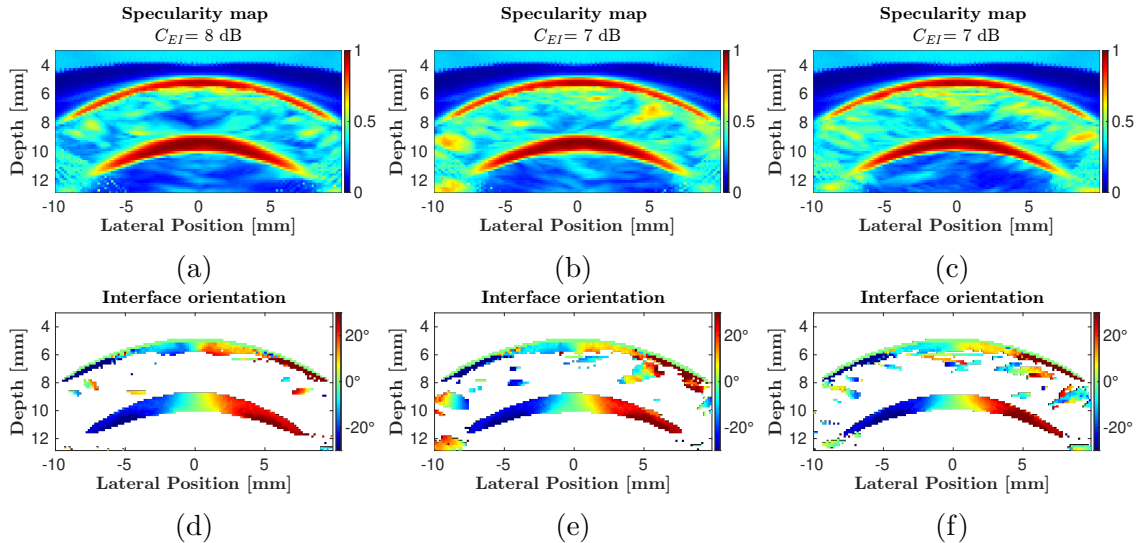


Figure 5.28: Specularity maps Ψ (top row images: panels a-c) and corresponding orientation maps $\tilde{\Theta}_l$ for pixel with specularity greater than 0.5 (bottom row images: panels d-f) for simulation configuration with curved bone interfaces. The diameter of the pore of the microstructure is $10 \mu\text{m}$. Panels a and d correspond to cortical porosity of 6%, panels b and e correspond to cortical porosity of 10% and panels c and f correspond to cortical porosity of 14%. Specular orientation is computed only for pixel with specularity greater than 0.5 with a scale ranging from -30 to 30° .

Curved interfaces. Same results are obtained for specularity of curved interfaces. In figure 5.28, specularity of pixels on the interfaces are very high (≥ 0.9). The specularity map shows probability values ranging from 0.85 to 0.99 on the first

bone interface. These values are nearly the same on the whole lateral extent of the interface from (e.g. for x varying from -10 to 10 mm). The corresponding specular orientation are ranging from -30 to 30 degrees. They correspond to the orientation of the local tangent at each point on the periosteal surface. The same variations are observed on the endosteal surface but with a lower lateral extent (from -7 mm to 7 mm). The narrower spread is due to the impossibility to retrieve backscattered echoes from some locations of the endosteal surface due to the high curvature of the interface increased by the refraction. This caused lower probability values. The corresponding specular orientations also ranges from -30 to 30 degrees. The estimated probability at the endosteal surface decreases slightly with porosity.

Within the cortical bone, probability values are low but higher than those found for flat interfaces (at some spots values approaches 0.5). Specularity within cortical bone increases with porosity and at 10 and 14% porosity some bright spot are observed inside bone cortex. However, the extent of these particular spots does not allow us to highlight a specular structure. Furthermore, the randomness of the corresponding estimated specular orientation tell us that these values are strong speckle contributions. These values are consistent with the simulation configuration Visibility of the endosteal surface is good: $C_{EI} = 7 \text{ dB}$ but lower than the corresponding configuration with flat interface. We can also remark that specularity of pixels below the internal interface are lower than specularity of pixels inside the cortex.

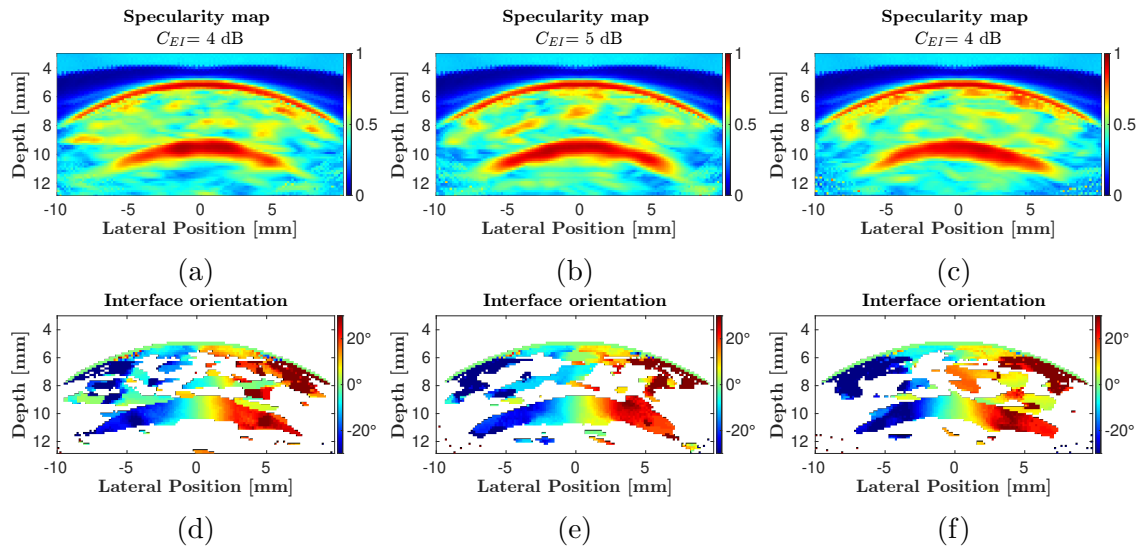


Figure 5.29: Same as figure 5.28 but the diameter of the pores is $30 \mu\text{m}$.

Specularity of the internal interface decreases with pore diameter (Figure 5.29 and 5.30). Specularity of pixels inside the cortex increases with pore diameter and for microstructure with pore diameter of $50 \mu\text{m}$, we obtain low C_{EI} values : $C_{EI} = 2 \text{ dB}$ for porosities of 6 and 10 % and $C_{EI} = 1 \text{ dB}$ for porosity of 14% (Figure 5.30).

Specular images compared to DAS image.

Planar interfaces. Figures 5.31, 5.32 and 5.33 show the reconstructed images for all simulated configurations with flat interfaces. The images reconstructed with DAS beamforming are compared to the images reconstructed with specular beamforming.

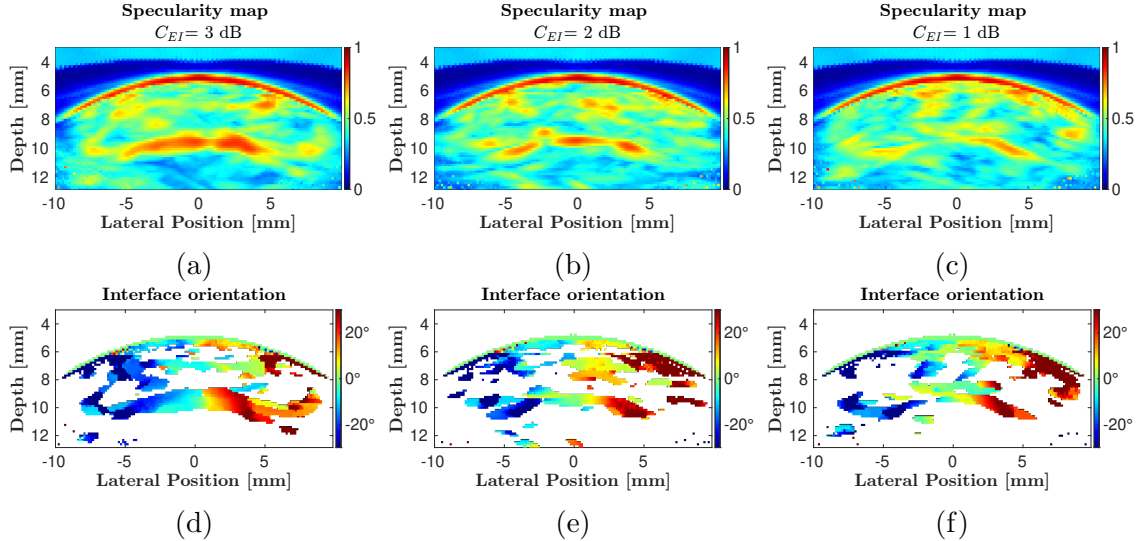


Figure 5.30: Same as figure 5.28 but the diameter of the pores is $50 \mu\text{m}$.

C_{EI} is given for each image. Qualitatively, we can see that with increasing porosity and individual pore diameter, speckle intensity inside bone increases and approaches the intensity of the endosteal interface.

For pore diameters of $10 \mu\text{m}$ (Figure 5.31), the endosteal interface is well distinguished from the inner bone cortex. For both beamforming algorithms, the periosteal and endosteal interfaces are clearly visible as bright zones centered respectively at 5 and 9 mm-depth as expected. C_{EI} values are ranging from 20 to 23 dB for DAS image and from 30 to 35 dB for specular images. C_{EI} values of specular images are always greater than those of DAS images. Specular beamforming improved the visibility of the endosteal interface by 10 dB. The texture of the interfaces is smoother in specular images and the speckle inside the cortex is lower.

For pore diameters of $30 \mu\text{m}$ (Figure 5.32), the endosteal interface is distinguished from the inner bone cortex. For both beamforming algorithms, the periosteal and endosteal interfaces are visible but the intensity of the speckle has increased. C_{EI} values are ranging from 10 to 13 dB for DAS images and from 16 to 18 dB for specular images. Here again, C_{EI} values of specular images are always greater than those of DAS images. Specular beamforming improved the visibility of the endosteal interface by 6 dB. In specular images, the texture of the interfaces is smoother and the speckle inside the cortex is lower.

For pore diameters of $50 \mu\text{m}$ (Figure 5.33), the endosteal interface is hardly distinguished from the inner bone cortex. For both beamforming algorithms, the periosteal interfaces is clearly visible but the intensity of the speckle increased and the endosteal interface vanished. For 6 and 10 % porosity, the interfaces are better defined in specular image but for 14% porosity, both DAS and specular images fail to reveal the endosteal surface. C_{EI} values are ranging from 3 to 5 dB for DAS images and from 4 to 8 dB for specular images.

Curved interfaces. Figures 5.34, 5.35 and 5.36 show the reconstructed images for configurations with curved interfaces.

For pore diameter of $10 \mu\text{m}$, for both beamforming algorithms, the periosteal and endosteal interfaces are clearly visible. With this geometry, due to the smaller

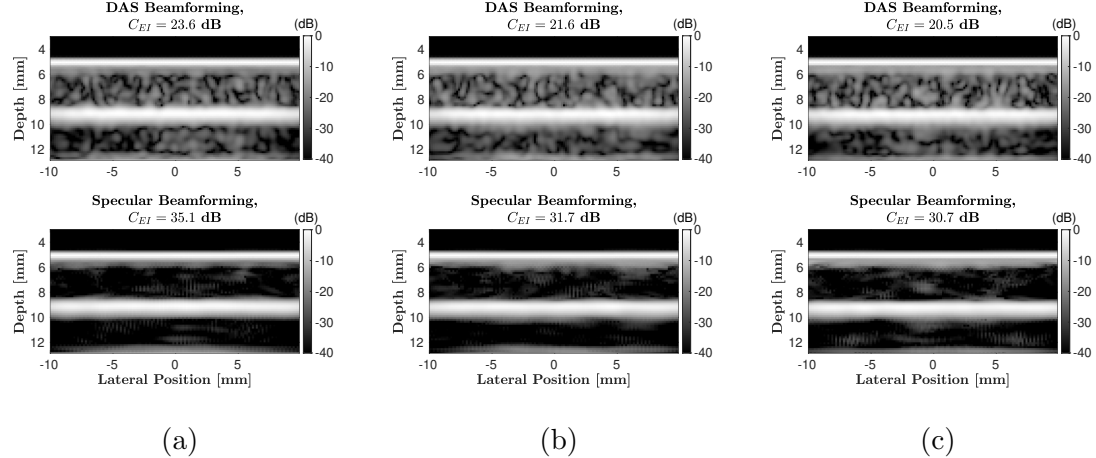


Figure 5.31: Reconstructed ultrasound images for simulated configurations with planar interfaces. Reconstruction was performed using a Delay-and-Sum (DAS) beamformer (top row images: panels a-c) and a specular beamformer (bottom row: panels d-f). The microstructure's pore diameter is 10 μm . Panels a and d correspond to a cortical porosity of 6%, panels b and e correspond to a cortical porosity of 10%, and panels c and f correspond to a cortical porosity of 14%. Each DAS image is reconstructed using an optimized receive f-number of 0.5. The intensity is log-compressed and displayed with a dynamic range of 40 dB.

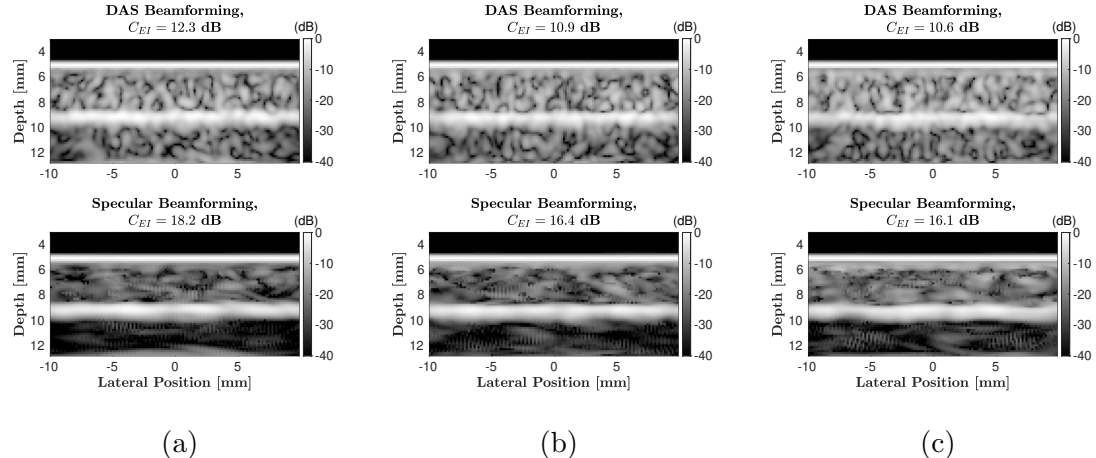


Figure 5.32: Same as in figure 5.31 except that pore diameter is 30 μm

transmitted energy of ultrasound at the periosteal interface (critical angle), C_{EI} values are smaller than for flat interfaces: ranging 20-23 dB for DAS images and ranging 26-29 dB for specular images. Endosteal visibility metric is increased by 6 dB. For specular images, speckle within the cortex is very low compared to DAS images.

For individual pore diameter of 30 μm , for both beamforming algorithms, the periosteal and endosteal interfaces are visible. C_{EI} values are ranging from 8 to 11 dB for DAS images and from 10 to 14 dB for specular images. Specular beamforming increased endosteal visibility metric by 2-3 dB.

For individual pore diameter of 50 μm , C_{EI} values are ranging from 2.7 to 5 dB for DAS images and from 1.9 to 5 dB for specular images. For cortical porosity of 6

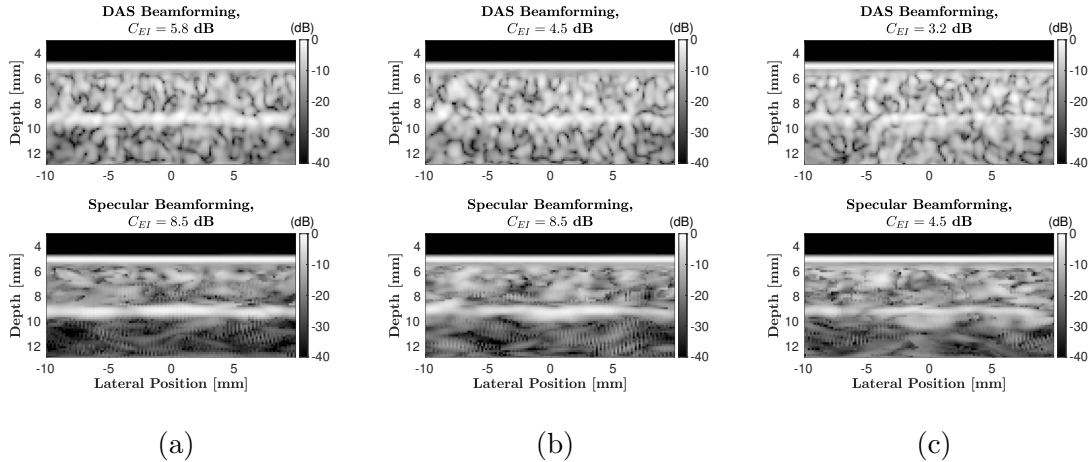
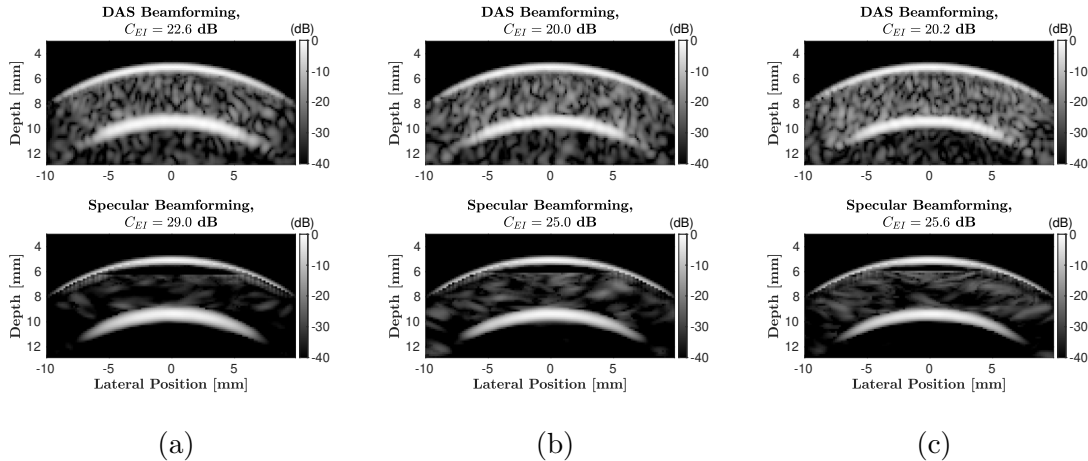

 Figure 5.33: Same as in figure 5.31 except that pore diameter is $50 \mu\text{m}$


Figure 5.34: Reconstructed ultrasound images for simulated configurations with curved interfaces. Reconstructions were performed using a Delay-and-Sum (DAS) beamformer (top row images: panels a-c) and a specular beamformer (bottom row: panels d-f). The microstructure's pore diameter is $10 \mu\text{m}$. Panels a and d correspond to a cortical porosity of 6%, panels b and e correspond to a cortical porosity of 10%, and panels c and f correspond to a cortical porosity of 14%. Each DAS image is reconstructed using an optimized receive f-number of 0.5. The intensity is log-compressed and displayed with a dynamic range of 40 dB.

and 10%, specular beamforming gives same C_{EI} as DAS beamforming. However, we can see from panel (a) of Figure 5.34 that the endosteum is qualitatively more visible in the specular image than in the DAS image. At 14%, C_{EI} of DAS image (2.7 dB) is better than C_{EI} of specular image (1.9 dB). However, we can not say visually that DAS image is better than specular image. This is due to the fact that at 10 and 14% porosity, the level of noise is very high and speckle inside cortex is considered as specular reflections. This is coherent with the results on the specularity of the reflections in Figure 5.30.

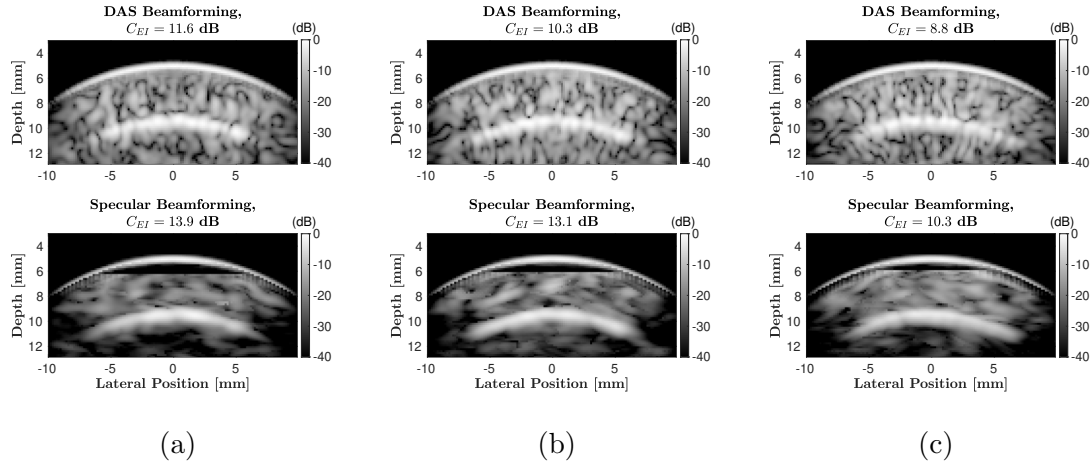


Figure 5.35: Same as in figure 5.34 except that pore diameter is 30 μm

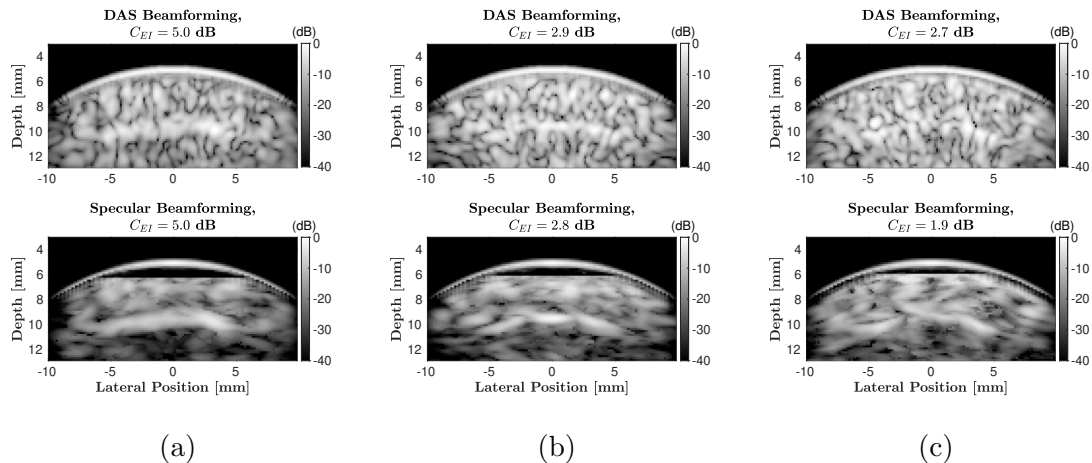


Figure 5.36: Same as in figure 5.34 except that pore diameter is 50 μm

5.4.3 Summary and discussion.

Quantitative results regarding the endosteal interface visibility are presented in Figure 5.37. For a constant porosity, C_{EI} values obtained from DAS images and specular images are plotted against the individual pore diameter of the simulation medium. In both beamforming algorithms, C_{EI} shows a decreasing trend with increasing pore diameter.

In the case of planar bone interfaces, specular beamforming consistently improves the C_{EI} contrast compared to DAS beamforming (panel 5.37a). For a pore diameter of 10 μm , there is an approximate 10 dB increase in contrast for all porosities. However, as the pore diameter increases, this enhancement diminishes, reaching nearly 3 dB at 50 μm . This diminishing trend is attributed to the correlation between speckle noise and the specular model. With a larger pore diameter, more speckle noise is considered as specular reflection (as observed in the increased specularity from Figures 5.25 to 5.27). Consequently, the speckle in specular images intensifies, resulting in a reduction in C_{EI} .

When bone interfaces are curved (panel 5.37b), the contrast increase is smaller. For a pore diameter of 10 μm , there is an approximately 6 dB increase across all

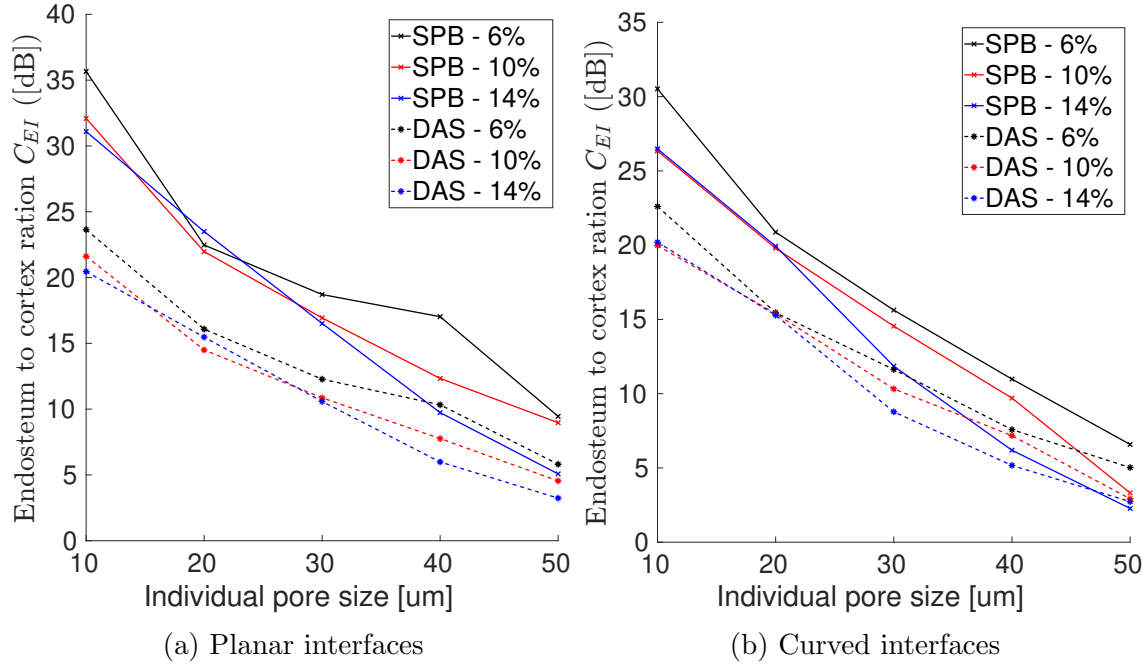


Figure 5.37: Comparison of endosteal interface visibility (C_{EI}) obtained with Delay-and-Sum (DAS) beamforming and specular beamforming. The metrics are plotted for each porosity considering individual pore size. Panel (a) illustrates the comparison for planar interfaces, while panel (b) shows the comparison for curved interfaces.

porosities and no increase for a pore diameter of 50 μm. This is attributed to a curved external interface reducing transmitted power and a curved internal interface decreasing power recorded by the probe.

We introduced the parameter η as the specular tolerance and experimented with various values. As illustrated in figure 5.38, when η is too close to zero, it results in high noise levels, leading to poor interface contrast. Conversely, if η is too close to 1, the specular signal from the true specular orientation Θ_l interferes destructively with off-axis signals, resembling a Delay-and-Sum (DAS) image. Therefore, choosing an appropriate tolerance is crucial. The optimal values determined for η were 0.1 for planar bone surfaces and 0.25 for curved bone surfaces. The higher value for curved geometry is due to the wider spread of the specular transform of a curved reflector

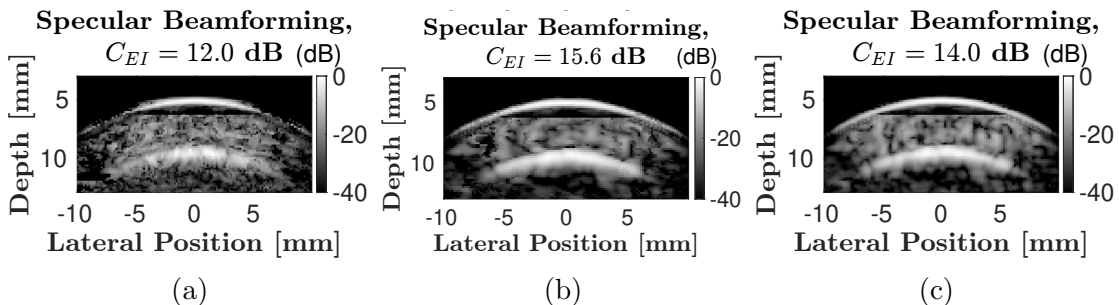


Figure 5.38: Demonstration of the impact of the parameter η on reconstructed ultrasound images. Three panels display images reconstructed with different η values: $\eta = 0$ in panel (a), $\eta = 0.25$ in panel (b), and $\eta = 0.5$ in panel (c). Each image corresponds to a pore size of 30 μm, with a cortical porosity of 6%.

compared to that of a planar reflector.

Maps of specularity (Ψ) and specular orientation ($\tilde{\Theta}_l$) provide valuable information into the nature of reflectors within the medium, offering information about their physical parameters. These maps are useful for detecting and characterizing specular structures. However, it is crucial to acknowledge that the resulting images may not be directly comparable to anatomical images, primarily due to the high specularity of non-specular structures (Ψ ranges from 0.2 to 0.5). Therefore, the use of I_{sp} provides a more natural ultrasound image, optimizing the signal-to-noise ratio.

In this simulation study, we simplified the representation of the bone layer by assuming homogeneity with pores having a single pore size. However, in reality, cortical microstructure is more complex, consisting of pores with various sizes. The objective of this chapter was to explore the influence of different pore sizes on specular imaging, considering diameters ranging from 10 to 50 μm . It is worth noting that for larger pore diameters, the cumulative scattering by all pores becomes excessive, posing challenges in obtaining clear ultrasound images of the cortex. For the application of specular beamforming to more realistic bone datasets, we turn to the next chapter, where the method is applied to ex-vivo and in-vivo bone ultrasound data.

5.5 Conclusion

In this chapter, we presented a beamforming algorithm grounded in the principles of reflection and refraction to enhance specular structures. Previous demonstrations illustrated that incorporating the physics of specular reflection in beamforming improves the visibility of planar specular objects within a homogeneous medium. We expanded the algorithm to address curved specular objects in a multi-layer heterogeneous medium, taking into account refraction. The goal was to decrease intra-cortical speckle noise and accentuate specular reflections from the medium.

The algorithm was implemented and tested on simulated bone datasets designed to replicate cortical bone with varying microstructures. We introduced a metric, denoted as C_{EI} , to quantify the visibility of the endosteal interface. Comparative analyses were conducted between the specular images generated using our algorithm and those obtained through DAS imaging. Notably, specular images exhibited enhanced visibility for microstructures characterized by pore diameters smaller than 50 μm .

In the next chapter we will apply the algorithm to ultrasound data with real cortical bone: ex-vivo and in-vivo.

Bibliography

- [1] Vincent Perrot, Maxime Polichetti, François Varray, and Damien Garcia. So you think you can DAS? A viewpoint on delay-and-sum beamforming. *arXiv:2007.11960 [eess]*, July 2020. arXiv: 2007.11960.
- [2] Jørgen Arendt Jensen. Medical ultrasound imaging. *Progress in Biophysics and Molecular Biology*, 93(1):153–165, January 2007.
- [3] M. Vogt, J. Opretzka, and H. Ermert. Parametric imaging of specular reflections and diffuse scattering of tissue from multi-directional ultrasound echo signal data. In *2008 IEEE Ultrasonics Symposium*, pages 1963–1966, November 2008. ISSN: 1051-0117.
- [4] Raja Sekhar Bandaru, Anders Rasmus Sornes, Jeroen Hermans, Eigil Samset, and Jan D’hooge. Delay and Standard Deviation Beamforming to Enhance Specular Reflections in Ultrasound Imaging. *IEEE Transactions on Ultrasonics, Ferroelectrics, and Frequency Control*, 63(12):2057–2068, December 2016. Conference Name: IEEE Transactions on Ultrasonics, Ferroelectrics, and Frequency Control.
- [5] Alfonso Rodriguez-Molares, Ali Fatemi, Lasse Løvstakken, and Hans Torp. Specular Beamforming. *IEEE Transactions on Ultrasonics, Ferroelectrics, and Frequency Control*, 64(9):1285–1297, September 2017. Conference Name: IEEE Transactions on Ultrasonics, Ferroelectrics, and Frequency Control.
- [6] Gayathri Malamal and Mahesh Raveendranatha Panicker. Towards Diffuse Beamforming For Specular Reflectors: A Pixel-Level Reflection Tuned Apodization Scheme For Ultrasound Imaging. In *2021 IEEE 18th International Symposium on Biomedical Imaging (ISBI)*, pages 415–418, April 2021. ISSN: 1945-8452.
- [7] Gayathri Malamal, Hans-Martin Schwab, and Mahesh Raveendranatha Panicker. Enhanced Needle Visualization With Reflection Tuned Apodization Based on the Radon Transform for Ultrasound Imaging. *IEEE Transactions on Ultrasonics, Ferroelectrics, and Frequency Control*, 70(11):1482–1493, November 2023. Conference Name: IEEE Transactions on Ultrasonics, Ferroelectrics, and Frequency Control.
- [8] Ryo Nagaoka, Jens E. Wilhjelm, and Hideyuki Hasegawa. Preliminary study on the separation of specular reflection and backscattering components using synthetic aperture beamforming. *Journal of Medical Ultrasonics*, 47(4):493–500, October 2020.
- [9] Gayathri Malamal and Mahesh Raveendranatha Panicker. On the physics of ultrasound transmission for in-plane needle tracking in guided interventions. *Biomedical Physics & Engineering Express*, 9(3):035018, March 2023. Publisher: IOP Publishing.
- [10] Guillaume Renaud, Pieter Kruizinga, Didier Cassereau, and Pascal Laugier. In vivo ultrasound imaging of the bone cortex. *Physics in Medicine & Biology*, 63(12):125010, June 2018. Publisher: IOP Publishing.

- [11] Huong Nguyen Minh, Juan Du, and Kay Raum. Estimation of Thickness and Speed of Sound in Cortical Bone Using Multifocus Pulse-Echo Ultrasound. *IEEE transactions on ultrasonics, ferroelectrics, and frequency control*, 67(3):568–579, 2020.
- [12] Damien Garcia. Make the most of MUST, an open-source Matlab UltraSound Toolbox. In *2021 IEEE International Ultrasonics Symposium (IUS)*, pages 1–4, September 2021. ISSN: 1948-5727.
- [13] M. Karaman, Pai-Chi Li, and M. O'Donnell. Synthetic aperture imaging for small scale systems. *IEEE Transactions on Ultrasonics, Ferroelectrics, and Frequency Control*, 42(3):429–442, May 1995. Conference Name: IEEE Transactions on Ultrasonics, Ferroelectrics, and Frequency Control.
- [14] Jørgen Arendt Jensen, Svetoslav Ivanov Nikolov, Kim Løkke Gammelmark, and Morten Høgholm Pedersen. Synthetic aperture ultrasound imaging. *Ultrasonics*, 44:e5–e15, December 2006.
- [15] Patrick Stähli, Maju Kuriakose, Martin Frenz, and Michael Jaeger. Improved forward model for quantitative pulse-echo speed-of-sound imaging. *Ultrasonics*, 108:106168, December 2020.
- [16] Emmanuel Bossy. SimSonic: free fdtd software for the simulation of ultrasonic waves propagation.
- [17] Amadou Sall Dia, Guillaume Renaud, Aida Hejazi Nooghabí, and Quentin Grimal. The influence of intra-cortical microstructure on the contrast in ultrasound images of the cortex of long bones: A 2D simulation study. *Ultrasonics*, 127:106831, January 2023.